Flat clathrin lattices: stable features of the plasma membrane

Joe Grove[a,b], Daniel J. Metcalf[c], Alex E. Knight[c], Silène T. Wavre-Shapton[a,*], Tony Sun[a], Emmanouil D. Protonotarios[d], Lewis D. Griffin[d], Jennifer Lippincott-Schwartz[e], and Mark Marsh[a]

[a]MRC Laboratory for Molecular Cell Biology and [d]CoMPLEX, University College London, London WC1E 6BT, United Kingdom; [b]Institute of Immunity and Transplantation, University College London, London NW3 2PF, United Kingdom; [c]Biophysics and Diagnostics, National Physical Laboratory, Teddington TW11 0LW, United Kingdom; [e]Cell Biology and Metabolism Program, Eunice Kennedy Shriver National Institute of Child Health and Human Development, National Institutes of Health, Bethesda, MD 20892

ABSTRACT **Clathrin-mediated endocytosis (CME) is a fundamental property of eukaryotic cells. Classical CME proceeds via the formation of clathrin-coated pits (CCPs) at the plasma membrane, which invaginate to form clathrin-coated vesicles, a process that is well understood. However, clathrin also assembles into flat clathrin lattices (FCLs); these structures remain poorly described, and their contribution to cell biology is unclear. We used quantitative imaging to provide the first comprehensive description of FCLs and explore their influence on plasma membrane organization. Ultrastructural analysis by electron and superresolution microscopy revealed two discrete populations of clathrin structures. CCPs were typified by their sphericity, small size, and homogeneity. FCLs were planar, large, and heterogeneous and present on both the dorsal and ventral surfaces of cells. Live microscopy demonstrated that CCPs are short lived and culminate in a peak of dynamin recruitment, consistent with classical CME. In contrast, FCLs were long lived, with sustained association with dynamin. We investigated the biological relevance of FCLs using the chemokine receptor CCR5 as a model system. Agonist activation leads to sustained recruitment of CCR5 to FCLs. Quantitative molecular imaging indicated that FCLs partitioned receptors at the cell surface. Our observations suggest that FCLs provide stable platforms for the recruitment of endocytic cargo.**

Monitoring Editor
Sandra L. Schmid
University of Texas
Southwestern Medical Center

Received: Jun 26, 2014
Revised: Aug 14, 2014
Accepted: Aug 18, 2014

INTRODUCTION

Clathrin-mediated endocytosis (CME) is the principal mechanism by which eukaryotic cells internalize cell surface constituents and cargoes from the extracellular environment. The molecular details of CME, borne out by 45 yr of microscopy, biochemical analysis, and genetic studies, have been synthesized into a standard model in which 1) adaptor proteins nucleate the assembly of a domed clathrin basketwork—a clathrin-coated pit (CCP)—on the cytoplasmic face of the plasma membrane; 2) this CCP specifically sequesters receptor cargoes as it undergoes progressive growth and invagination to form a spherical cavity connected to the cell surface by a narrow membrane neck; 3) a scission machinery, involving the GTPase dynamin, severs the neck to generate an intracellular clathrin-coated vesicle (CCV) measuring ~100 nm in diameter; and 4) coordinated disassembly of the clathrin basketwork liberates the underlying vesicle, allowing delivery of its cargo via fusion with the endosomal network. There is a wealth of evidence to support this model, and the sequential molecular interactions that drive the process are relatively well understood (McMahon and Boucrot, 2011; Taylor *et al.*, 2011; Brodsky, 2012). However, numerous microscopy studies have revealed a heterogeneous array of membrane-associated clathrin coats, including large, flat structures, variably referred to as patches, plaques, or flat clathrin lattices, that are not considered in this standard model.

This article was published online ahead of print in MBoC in Press (http://www.molbiolcell.org/cgi/doi/10.1091/mbc.E14-06-1154) on August 27, 2014.

*Present address: Molecular Medicine Section, National Heart and Lung Institute, Imperial College London, London SW7 2AZ, United Kingdom.

Address correspondence to: Joe Grove (j.grove@ucl.ac.uk), Mark Marsh (m.marsh@ucl.ac.uk).

Abbreviations used: CCP, clathrin-coated pit; CCS, clathrin-coated structure; CCV, clathrin-coated vesicle; CME, clathrin-mediated endocytosis; FCL, flat clathrin lattice; GPCR, G protein–coupled receptor.

Supplemental Material can be found at:
http://www.molbiolcell.org/content/suppl/2014/08/25/mbc.E14-06-1154v1.DC1.html

Various techniques allow the preparation of plasma membrane sheets in such a way that the cytoplasmic surface can be examined en face by electron microscopy (EM; Heuser, 1980, 2000; Sanan and Anderson, 1991). Using these techniques, early ultrastructural studies of different cell types revealed a variety of clathrin-coated structures (CCSs), including small spherical CCPs, which later came to be understood in the standard model just described, and much larger, irregularly shaped, flat clathrin lattices (FCLs; Heuser, 1980; Maupin and Pollard, 1983). It was initially suggested that these planar CCSs might be an intermediate form of CCP (Heuser, 1980; Larkin *et al.*, 1986). However, it became clear that in some cell types, FCLs reach sizes much greater than can be resolved into a single CCV (Heuser, 1980; Miller *et al.*, 1991; Sanan and Anderson, 1991). Furthermore, invaginating structures were observed emanating from the periphery of FCLs (Maupin and Pollard, 1983; Heuser, 1989; Pumplin and Bloch, 1990; Marsh and McMahon, 1999; Hinrichsen *et al.*, 2006), suggesting that they may generate CCVs via rearrangement of their basketwork or nucleation of de novo clathrin assembly (Heuser, 1989; Otter and Briels, 2011). Subsequent EM studies implicated FCLs in the internalization of specific endocytic cargoes, cellular adhesion, and the formation of phagocytic cups (Aggeler and Werb, 1982; Maupin and Pollard, 1983; Nicol and Nermut, 1987; Pumplin and Bloch, 1990; Miller *et al.*, 1991; Sanan and Anderson, 1991; Signoret *et al.*, 2005; Akisaka *et al.*, 2008). Nonetheless, FCLs have remained a poorly defined facet of plasma membrane biology.

The advent of live-cell microscopy with genetically encoded fluorescent protein tags in the late 1990s allowed the kinetics of CME to be examined (Gaidarov *et al.*, 1999). Such studies have been instrumental in defining the sequence of molecular events that drive the standard model of CME (Merrifield *et al.*, 2002, 2005; Rappoport and Simon, 2003; Ehrlich *et al.*, 2004; Loerke *et al.*, 2009; Henne *et al.*, 2010; Taylor *et al.*, 2011). However, the diffraction properties of light limit the resolution of standard fluorescence microscopes to ~300 nm, making it difficult to distinguish CCSs based on size and geometry. Therefore, to aid systematic analysis, there has been a tendency to either use cell types that exclusively exhibit homogeneous CCP-type structures or analytically eschew CCSs that do not possess the typical characteristics of CCPs (transient, diffraction-limited spots; Merrifield *et al.*, 2002; Ehrlich *et al.*, 2004; Loerke *et al.*, 2009). Consequently, no report has unequivocally examined FCLs and their dynamic characteristics.

A number of live-imaging studies observed comparatively large CCSs that may represent FCLs (Gaidarov *et al.*, 1999; Rappoport *et al.*, 2004; Bellve *et al.*, 2006), and data suggest that these are able to generate multiple successive cargo-laden CCVs (Merrifield *et al.*, 2005; Taylor *et al.*, 2011). Saffarian *et al.* (2009) described a population of stable CCSs termed clathrin plaques (a terminology appropriated from the original EM literature; Maupin and Pollard, 1983; Pumplin and Bloch, 1990). The assembly and resolution of clathrin plaques were dependent on actin, and, unlike CCPs, plaques internalized as a flat coat without prior invagination. The authors equated these structures to large, flat clathrin coats previously observed by EM; however, fluorescence and ultrastructural data suggested that these plaques are relatively small (approximately three times the size of a CCP; Saffarian *et al.*, 2009). Hence there has yet to be a direct reconciliation of the heterogeneous CCSs viewed by EM with live-cell fluorescence microscopy.

In this study we used multimodal microscopy to revisit FCLs and define their principal characteristics. Quantitative EM of plasma membrane sheets from various cell types demonstrated two morphologically distinct populations of clathrin structures: small, uniform CCPs and large, heterogeneous FCLs. Superresolution fluorescence microscopy of fixed whole cells confirmed these observations. Live-cell total internal reflection fluorescence (TIRF) microscopy corroborated the coexistence of distinct structures. CCPs exhibited transient lifetimes that culminated in a peak of dynamin recruitment; FCLs did not conform to the typical dynamics of CME, being extremely long lived, with persistent recruitment of dynamin.

The chemokine receptor CCR5 undergoes CME (Signoret *et al.*, 2005); therefore we used this model system to investigate the relevance of FCLs to plasma membrane biology. Live-cell TIRF imaging revealed progressive and sustained association of CCR5 with FCLs after stimulation with chemokine ligand. Quantitative dual-color superresolution microscopy suggests that FCLs are able to selectively partition CCR5 at the cell surface. As such, FCLs may provide stable sites for the recruitment of endocytic cargo such as G protein–coupled receptors (GPCRs).

RESULTS

Flat clathrin lattices are a discrete population of nonclassical CCSs

The distinctive polygonal basketwork of CCSs make them easy to identify and particularly amenable to ultrastructural analysis (Heuser, 1980). We first evaluated clathrin heterogeneity in a variety of cell lines by preparing ventral (bottom) and dorsal (top) plasma membrane sheets for EM. Concordant with the standard model of CME, we observed abundant small, round structures characteristic of CCPs. In some cell types (e.g., HEK-293T and BSC-1 cells), these structures predominated (Figure 1A, i and ii, and unpublished data). However, other cell types (e.g., HeLa and CHO cells) also formed large, irregular FCLs (Figure 1Aiii and Supplemental Figure S4; examples of ventral membrane sheets from HEK-293T and HeLa cells are provided in Supplemental Figures S1 and S2).

We manually segmented discrete CCSs in images of replicate membrane sheets from HEK-293T and HeLa cells, allowing quantitative analysis of clathrin morphology. Scatter plots displaying the surface area and circularity of individual CCSs associated with the ventral plasma membrane are shown in Figure 1B. CCPs are represented by a well-defined population of small, highly circular structures with a two-dimensional surface area of ~10,000 and ≤30,000 nm^2. These values are in good agreement with prototypical CMEs, in which progressive assembly and invagination of CCPs give rise to spherical vesicles 100–200 nm in diameter (McMahon and Boucrot, 2011). Whereas these CCPs predominated in HEK-293T, HeLa cells exhibited greater heterogeneity, with an additional population of larger structures representing FCLs (Figure 1B). The surface area of individual FCLs was often >100,000 nm^2, and they were typified by an inverse relationship between size and circularity, a reflection of their irregular shape (Figure 1Aiii).

To better represent this cell-type-specific phenotype, we calculated the relative frequency of small (<30,000 nm^2), medium (30,000–100,000 nm^2), and large (>100,000 nm^2) CCSs associated with the ventral and dorsal plasma membrane (Figure 1C). Small CCP-type structures accounted for >90% of CCSs in HEK-293T cells, whereas large structures were virtually absent. In contrast, FCLs (defined as structures >100,000 nm^2) represented ~35% of the CCSs on the ventral surface of HeLa cells. There have been conflicting reports as to whether FCLs only reside on the ventral surface of cells grown in adherent culture (Maupin and Pollard, 1983; Miller *et al.*, 1991; Sanan and Anderson, 1991; Damke *et al.*, 1994; Lamaze *et al.*, 2001; Signoret *et al.*, 2005; Akisaka *et al.*, 2008; Saffarian *et al.*, 2009; Vassilopoulos *et al.*, 2014). Our quantitative analysis clearly demonstrates that FCLs can form on the dorsal surface of HeLa cells, albeit

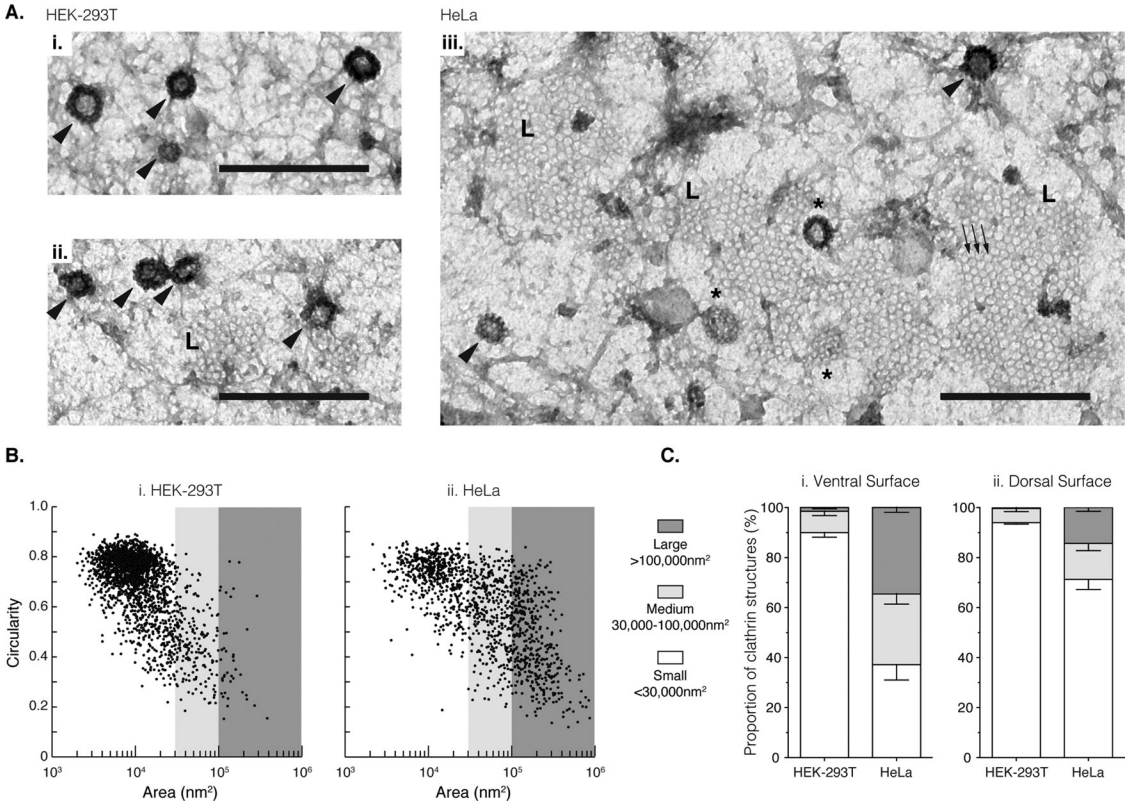

FIGURE 1: An electron microscopy survey of clathrin heterogeneity. Plasma membrane sheets from the ventral and dorsal cell surfaces were prepared for electron microscopy. (A) Representative images of the ventral plasma membrane of HEK-293T (i, ii) and HeLa cells (iii); Scale bar, 500 nm. In HEK-293T cells, small, homogeneous CCPs (arrowheads) predominate. HeLa cells show similar CCPs but had a propensity to also form large FCLs (L), largely composed of hexagonal clathrin basketwork (arrows). FCLs often displayed budding structures at their periphery (asterisks), which appeared morphologically similar to classical CCPs. (B) Morphometric analysis of clathrin heterogeneity was performed by manual image segmentation (see *Materials and Methods*). Scatter plots display the circularity and two-dimensional surface area of individual CCSs from the ventral surface of i) HEK-293T ($n = 2256$ structures) and ii) HeLa cells ($n = 1329$ structures). Shading indicates CCSs defined as small, <30,000 nm^2 (white); medium, 30,000–100,000 nm^2 (light gray); or large, >100,000 nm^2 (dark gray). (C) Stacked histograms expressing the relative frequency of small, medium, and large structures on the ventral (i) and dorsal (ii) surface of HEK-293T and HeLa cells; $n = 24$ and 19 cells, respectively, surveyed across three independent experiments. Error bars indicate SEM.

at approximately twofold lower frequency (Figure 1C), and we also observed dorsal FCLs in CHO cells (Signoret *et al.*, 2005; Supplemental Figure S6).

When viewed by EM, the two-dimensional projection of a deeply invaginated CCP and CCV generates a characteristic ring of low electron intensity, as exemplified in Supplemental Figure S3B. This is a consequence of the electron beam passing through multiple surfaces as it transits a CCP (Supplemental Figure S3A). This feature provides a surrogate measure of sphericity, allowing us to evaluate the topography of CCSs (Supplemental Figure S3B). We measured the radial electron intensity profiles of CCPs and FCLs in both HEK-293T and HeLa cells. CCPs (defined as structures with area <30,000 nm^2 and circularity >0.7) exhibited W-shaped profiles indicative of a spherical geometry (Supplemental Figure S3C). These profiles measured ~100 nm in diameter, and their characteristics were independent of cell type, further suggesting that classical CME produces uniform CCPs/CCVs in both HEK-293T and HeLa cells.

To accommodate membrane curvature, pentagons must be incorporated into the hexagonal clathrin basketwork (Kanaseki and Kadota, 1969; Smith *et al.*, 1998; Marsh and McMahon, 1999; Otter and Briels, 2011). FCLs were largely composed of a hexagonal arrangement of clathrin (Figure 1Aiii), and there was little variation in the electron intensity profile across their surface (Supplemental Figure S3C), indicating a planar topography. However, small, round CCP-like formations were often observed at the periphery of FCLs (Figure 1Aiii and Supplemental Figure S3D). The mean electron intensity profile across these budding features appeared very similar to that of CCPs with a diameter of ~100 nm (Supplemental Figure S3E), and this is consistent with the notion that FCLs are capable of generating CCVs that are indistinguishable from those produced by standard CME (Marsh and McMahon, 1999; Merrifield *et al.*, 2005; Bellve *et al.*, 2006; Hinrichsen *et al.*, 2006; Mettlen *et al.*, 2010; Taylor *et al.*, 2011; Lampe *et al.*, 2014).

EM provides a very high resolution view of the plasma membrane; however, the preparation of membrane sheets requires mechanical shearing or tearing of cells, which might introduce artifacts. This is a particular concern, given that FCLs might act as sites of adhesion on the ventral surface of cells (Maupin and Pollard, 1983; De Deyne *et al.*, 1998; Akisaka *et al.*, 2003), and shearing techniques might enrich for membranes with abundant adhesion sites and thus FCLs (Akisaka *et al.*, 2003). Sample preparation for fluorescence microscopy is not prone to such artifacts, yet the resolution of standard microscopy techniques is limited to ~300 nm by the intrinsic diffraction of light, making it difficult to discern individual CCSs. Therefore, to corroborate our EM observations, we used superresolution direct stochastic optical reconstruction microscopy (dSTORM; capable of

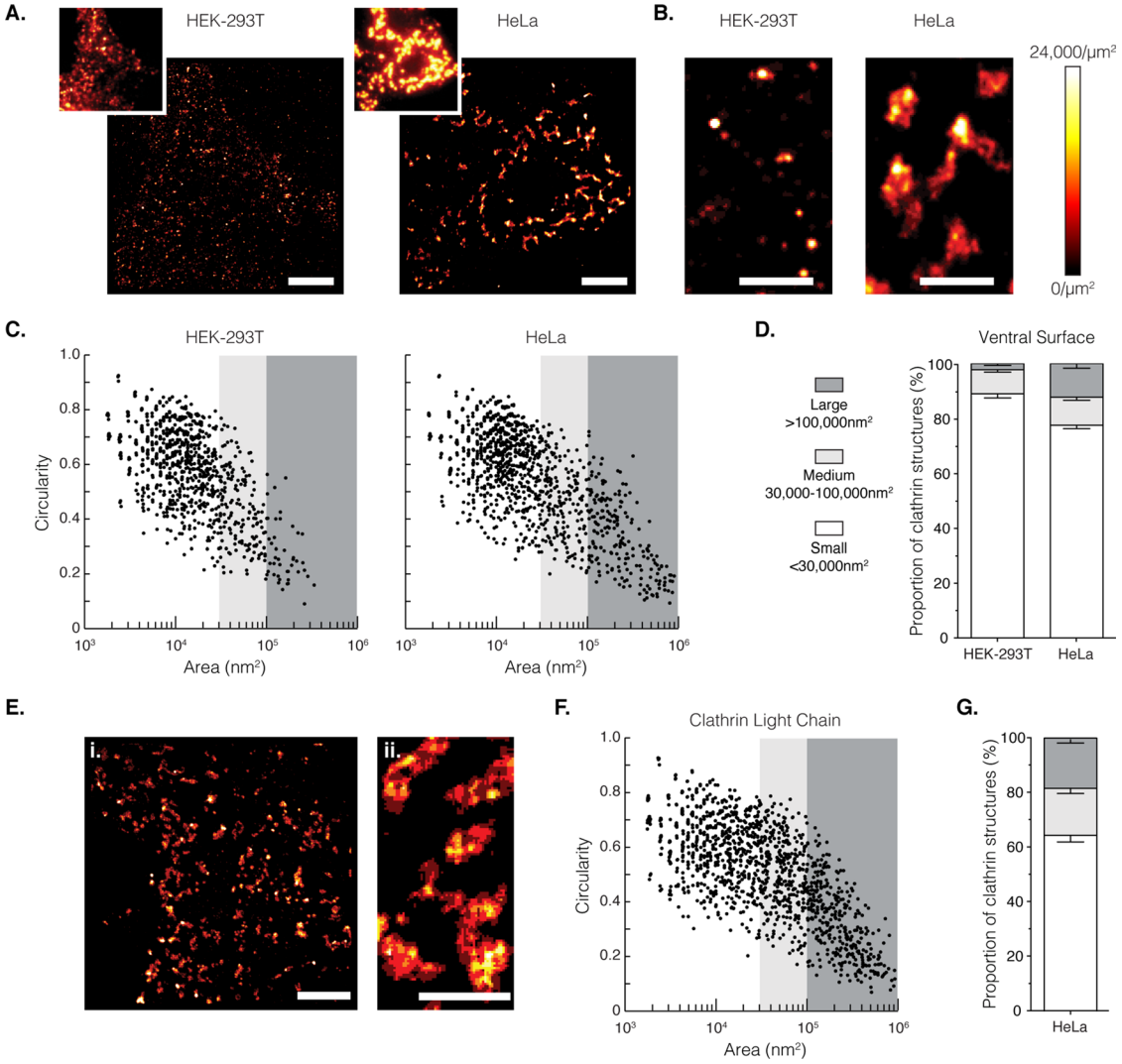

FIGURE 2: A superresolution microscopy survey of clathrin heterogeneity. Whole fixed cells were permeabilized and labeled with a mouse anti–clathrin heavy chain mAb, followed by secondary anti-mouse Alexa Fluor 647. We imaged CCSs on the ventral cell surface by dSTORM using TIRF illumination. (A) dSTORM superresolution images of CCSs in HEK-293T and HeLa cells. Images were reconstructed using a 25-nm pixel size; scale bar, 4 μm. Insets display standard diffraction-limited TIRF images of the same area. (B) Enlarged areas from dSTORM images in A, displaying small, round CCPs in HEK-293T and large, pleomorphic FCLs in HeLa cells; scale bar, 1 μm. Heat map intensity scale indicates density of localizations/μm^2. (C) Morphometric analysis of clathrin heterogeneity was performed by automated image segmentation (see *Materials and Methods*). Scatter plots display the circularity and two-dimensional surface area of individual CCSs from HEK-293T and HeLa cells; each plot displays 2000 representative structures. Color coding indicates CCSs defined as small, <30,000 nm^2 (white); medium, 30,000–100,000 nm^2 (light gray); or large, >100,000 nm^2 (dark gray). (D) Stacked histograms displaying the relative frequency of small, medium, and large structures in HEK-293T and HeLa cells from $n = 8$ and 13 cells, respectively, surveyed across three independent experiments; error bars indicate SEM. (E) HeLa cells were stained with rabbit anti–clathrin light chain polyclonal serum, followed by secondary anti-rabbit Alexa Fluor 647. Representative dSTORM image (i). The image was reconstructed with a 25-nm pixel size; scale bar, 4 μm. An enlarged area is shown in ii; scale bar, 1 μm. (F, G) Morphometric analysis of CCSs stained with clathrin light chain; the scatter plot displays 2000 structures from $n = 4$ cells surveyed in one experiment; error bars indicate SD from the mean.

achieving resolutions of ~20 nm; Bates *et al.*, 2007; Heilemann *et al.*, 2008) to study clathrin heterogeneity in whole cells. We labeled endogenous clathrin heavy chain in fixed and permeabilized HEK-293T and HeLa cells with a monoclonal antibody followed by a polyclonal secondary antibody conjugated to Alexa Fluor 647. dSTORM was performed on the ventral surface of the cells under TIRF illumination.

dSTORM recapitulated our ultrastructural studies; HEK-293T cells possessed numerous small puncta of clathrin, whereas HeLa cells displayed large, heterogeneous arrays (Figure 2, A and B). Automated segmentation allowed us to perform morphometric analysis as in Figure 1, B and C. Despite the lower resolution of dSTORM compared with EM, a distinct population of small, round CCPs was discernible in both cell types, whereas large, irregular FCLs were only common in HeLa cells (Figure 2C). We independently confirmed these observations in HeLa cells stained with a polyclonal anti–clathrin light chain antibody (Figure 2, E–G) and anti–α-adaptin (unpublished data). Frequency analysis of CCSs in HEK-293T cells by dSTORM was similar to data generated by EM (compare Figures 2D and 1Ci). In contrast, FCLs were less frequent

on the ventral surface of whole HeLa cells assessed by dSTORM (10–20%; Figure 2, D and G) when compared with membrane sheets imaged by EM (35%; Figure 1Ci). However, given the likelihood of artifactually enriching for FCLs during EM sample preparation (Akisaka *et al.*, 2003), superresolution imaging of whole cells is likely to provide a more reliable representation of the frequency of CCSs. Furthermore, dSTORM permits the systematic survey of thousands of structures across large fields of view.

By quantifying structures in whole cells, we can generate an accurate estimate of the proportion of total cell surface clathrin found within small or large structures. FCLs (defined as >100,000 nm^2) accounted for ~75% of clathrin associated with the ventral plasma membrane of HeLa cells, compared with ~20% in HEK-293T (unpublished data). This equates to ~8% of HeLa cell plasma membrane being covered in FCLs; this figure is remarkably similar to an estimate based on EM of primary rat myotubes (Pumplin and Bloch, 1990). As a point of comparison, CCPs cover only ~1.5% of HeLa cell plasma membrane. Almost identical data were derived from morphometric analysis of FCLs in CHO cells (see later discussion and Supplemental Figure S4).

In summary, we used high-resolution EM and dSTORM imaging to demonstrate two morphologically distinct subsets of clathrin-coated structures. CCPs were small (100–150 nm in diameter) and spherical, with a uniform geometry. In contrast, FCLs did not conform to the classical model of CME, being large, irregular, and planar structures with occasional CCP-like invaginations at their periphery. Whereas CCPs were ubiquitous, FCLs were present only in certain cell lines; however, in these cells, FCLs accounted for the vast majority of clathrin associated with the plasma membrane.

Flat clathrin lattices are long lived

Since the development of live-cell fluorescence and TIRF microscopy, numerous studies have examined the dynamics of plasma membrane CCSs (Gaidarov *et al.*, 1999; Rappoport and Simon, 2003; Ehrlich *et al.*, 2004; Merrifield *et al.*, 2005; Saffarian *et al.*, 2009). However, no study has yet reconciled ultrastructural observations of clathrin heterogeneity with live imaging to directly address FCL dynamics. HeLa cells possess extensive arrays of FCLs, many of which cross the intrinsic diffraction limit of optical microscopy (Figures 1 and 2), making them particularly amenable to analysis by live TIRF imaging.

FCLs contain abundant clathrin light chain (Figure 2E), and therefore we examined their dynamics by transiently transfecting HeLa cells with light chain tagged with red fluorescent protein (LCb-RFP). Of importance, exogenous expression of clathrin light chain did not alter CCS frequency or morphology, as assessed by superresolution microscopy (unpublished data). We also introduced enhanced green fluorescent protein–tagged dynamin-2 (Dyn-2–EGFP), the mechanoenzyme largely responsible for the scission of CCVs (McMahon and Boucrot, 2011). Dynamin exhibits moderate association with nascent CCSs, where it is believed to regulate maturation (Macia *et al.*, 2006; Loerke *et al.*, 2009; Taylor *et al.*, 2012; Aguet *et al.*, 2013); thereafter, a further stage of intense dynamin recruitment occurs as it assembles around the membranous neck of CCPs before vesicle scission (Taylor *et al.*, 2011, 2012; Grassart *et al.*, 2014). As such, dynamin recruitment provides information on the maturation of CCSs and registers individual endocytic events. We therefore reasoned that monitoring levels of Dyn-2–EGFP would allow us to better describe the lifetime of classical CCPs and possibly afford a view of vesicle scission events occurring at FCLs.

As expected following our observations by EM and dSTORM, large, intense CCSs representing FCLs were easily discernible by live TIRF imaging of HeLa cells expressing LCb-RFP. FCLs were notable for their stability, displaying no lateral mobility, very little variation in morphology, and typically persisting beyond the time frame of our experiments (10-min acquisition at 0.33 frame/s; Figure 3A and Figure 3 Video 1). On closer examination of the data, numerous transient CCP-type events were also apparent (highlighted with arrows in Figure 3 Video 1). We quantified the dynamics of CCSs in HeLa cells using an unbiased tracking algorithm previously validated for clathrin studies (Jaqaman *et al.*, 2008; Loerke *et al.*, 2009; Cocucci *et al.*, 2012; Aguet *et al.*, 2013; Figure 3B). A large proportion of events were very short lived (<20s) and are likely to represent small, abortive CCPs and endosomal structures that transiently move into the TIRF field (Ehrlich *et al.*, 2004; Loerke *et al.*, 2009). A further population of short-lived events (20–300 s) principally consisted of diffraction-limited CCP-type structures. Very few events displayed an intermediate lifetime of 300–600 s; however, stable FCL events with lifetimes beyond the duration of our experiments (>600 s) accounted for ~12% of all clathrin events. Representative kymographs of transient pits and persistent lattice events are shown in Figure 3C.

The short-lived CCP events possessed archetypal Dyn-2–EGFP recruitment: gradual accumulation of signal in parallel to LCb-RFP, in agreement with an early role for dynamin in CME (Macia *et al.*, 2006; Loerke *et al.*, 2009; Taylor *et al.*, 2012; Aguet *et al.*, 2013), followed by an intense peak concomitant with loss of the clathrin signal, indicating CCV scission and subsequent uncoating or movement away from the TIRF field (Figure 3C and Figure 3 Video 1). In striking contrast, FCLs possessed a continuous Dyn-2–EGFP signal, indicating persistent recruitment (Figure 3, A and C, and Figure 3 Video 1). This hints that dynamin may play a role in the maturation and/or maintenance of planar CCSs, as well as in regulation of invaginated CCPs as previously proposed (Macia *et al.*, 2006). The GTPase activity of dynamin is believed to be necessary both for its early role in CCS development and for vesicle scission (Taylor *et al.*, 2012); despite this, the catalytically inactive Dyn-2–K44A-EGFP (Damke *et al.*, 1994) was able to associate with FCLs (unpublished data), suggesting that the dynamin GTP cycle does not regulate recruitment to FCLs. Aware that overexpression of Dyn-2–EGFP might drive aberrant recruitment to CCSs, we evaluated the distribution of endogenous dynamin in fixed HeLa cells by immunofluorescence. TIRF microscopy confirmed association of endogenous dynamin with large, intense FCL structures (Figure 3Di). Superresolution dSTORM imaging revealed a punctate distribution of dynamin, which is reminiscent of previous immunogold EM observations of dynamin associated with flat clathrin structures (Damke *et al.*, 1994; Warnock *et al.*, 1997) and may indicate that it is recruited to discrete sites within the latticework (Figure 3Dii). In conclusion, commensurate with their distinct morphology, FCLs are also kinetically distinct from classical CCPs.

Flat clathrin lattices are molecularly dynamic

The molecular exchange of clathrin triskelia between the cytosolic pool and CCSs at the plasma membrane remains a contentious topic. Various reports used fluorescence recovery after photobleaching (FRAP) to demonstrate turnover of the constituents of CCSs (Wu *et al.*, 2001; 2003; Mettlen *et al.*, 2010; Taylor *et al.*, 2012), although interpretation of these results is confounded by the intrinsic transitory nature of CCPs. Others studies of pharmacologically arrested CCPs found no fluorescence recovery (Macia *et al.*, 2006; Kleist *et al.*, 2011). Furthermore, completion of CME requires the active disassembly of clathrin from CCVs by Hsc70 and auxillin/GAK (Schlossman *et al.*, 1984; Greene and Eisenberg, 1990; Ungewickell *et al.*, 1995; Böcking *et al.*, 2011). The latter

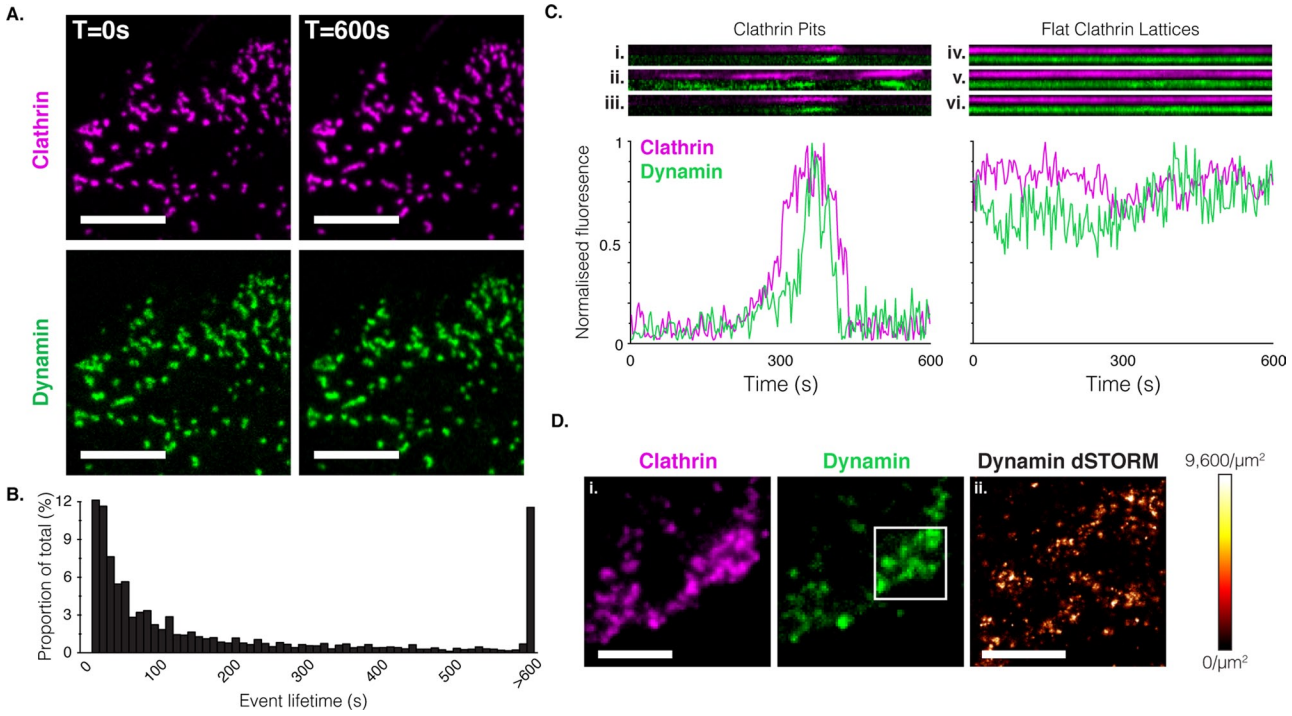

FIGURE 3: Flat clathrin lattices are long lived. HeLa cells expressing LCb-RFP and Dyn-2–EGFP were imaged by TIRF microscopy for 10 min at 0.33 frame/s. FCLs appeared as large, intense clathrin structures that persisted beyond the period of acquisition. (A) Stills taken from the beginning ($T = 0$ s) and end ($T = 600$ s) of a representative time course. Images display the cell surface distribution of clathrin (magenta) and dynamin (green); scale, 10 μm. (B) The lifetime of clathrin events was quantified using an automated tracking algorithm (see *Materials and Methods*). The histogram displays the distribution of CCS lifetimes using 9-s-wide bins, based on 6628 events from three acquisitions across two independent experiments. (C) Representative kymographs displaying fluorescent traces from CCPs, including "hot-spot"-type dynamics (ii), and FCLs. Line plots display normalized fluorescence intensity from the lowermost kymographs (iii, vi). Examples were chosen from transient and long-lived structures identified using the tracking algorithm. (D) Whole fixed HeLa cells were permeabilized and labeled with mouse anti–clathrin heavy chain mAb and goat anti–dynamin-2 polyclonal IgG, followed by secondary anti-mouse Alexa Fluor 488 and anti-goat Alexa Fluor 647. (i) Images of the cell surface distribution of clathrin (magenta) and dynamin (green) were acquired using standard TIRF microscopy; scale bar, 5 μm. The distribution of dynamin was also examined by superresolution microscopy. (ii) A dSTORM reconstruction of the boxed area from i; the image was reconstructed using a 25-nm pixel size; scale bar, 2 μm. Heat map intensity scale indicates density of localizations/μm².

observations suggest that the basketwork of maturing CCPs does not undergo molecular exchange. The long lifetimes of FCLs make them particularly well suited to FRAP analysis. Therefore we examined clathrin and dynamin turnover by simultaneous photobleaching of LCb-RFP and Dyn-2–EGFP within selected groups of FCLs. Of importance, the interaction between clathrin light and heavy chain is very stable, such that the molecular dynamics of LCb-RFP faithfully represents the behavior of clathrin triskelia subunits (Hoffmann *et al.*, 2010; Brodsky, 2012). Clathrin fluorescence displayed gradual but sustained recovery, reaching 50% after ~115 s (Figure 4 and Figure 4 Video 1), demonstrating that subunits of the FCL basketwork are being exchanged with the cytosolic pool. Dynamin recovery also indicated turnover, although with much faster kinetics; the signal recovered to 50% in <9 s. This transitory recruitment may be analogous to the "flickering" association of dynamin with maturing CCPs that precedes the stable assembly of the scission machinery, as proposed by Taylor *et al.* (2012) or the abortive recruitment of dynamin to endocytically immature CCSs recently suggested by Grassart *et al.* (2014). Mean fluorescence recovery profiles (Figure 4B) show that LCb-RFP signal recovers to only ~65%, indicating that a significant proportion of clathrin within FCLs is not available for exchange; on the contrary, the vast majority of dynamin was mobile, with fluorescence reaching >90% recovery within ~80 s.

The turnover of clathrin from FCLs may occur via passive exchange with the cytosolic pool or through active processes such as the quasi-enzymatic disassembly of the clathrin basketwork by Hsc70 and auxilin/GAK (Schlossman *et al.*, 1984; Greene and Eisenberg, 1990; Ungewickell *et al.*, 1995; Böcking *et al.*, 2011). To discriminate between these scenarios, we evaluated FCL FRAP in cells depleted of ATP. Recovery of clathrin fluorescence was prevented in the absence of cellular energy (Figure 4B and Figure 4 Videos 1 and 2), concordant with active turnover of FCLs. In contrast, recovery of dynamin remained largely unaffected by ATP depletion (Figure 4 Videos 1 and 2). This evokes a scenario in which clathrin, an integral component of FCLs, requires active remodeling, whereas dynamin is fleetingly recruited from the cytosolic pool to FCLs, presumably via transient protein–protein interactions. In summary, despite their structural stability (Figure 3), FCLs are dynamic molecular assemblies.

Flat clathrin lattices regulate the cell surface distribution of CCR5

CCR5 is a chemokine receptor responsible for chemotactic migration in a number of leucocytes, including T-cells and macrophages, and, of note, is also a coreceptor for human immunodeficiency viruses (HIV; Dragic *et al.*, 1996; Oppermann, 2004). CCR5 is a seven-transmembrane domain GPCR for which ligand binding and activation triggers $G\alpha_{(i)}/G\beta$ signaling. Subsequent phosphorylation of

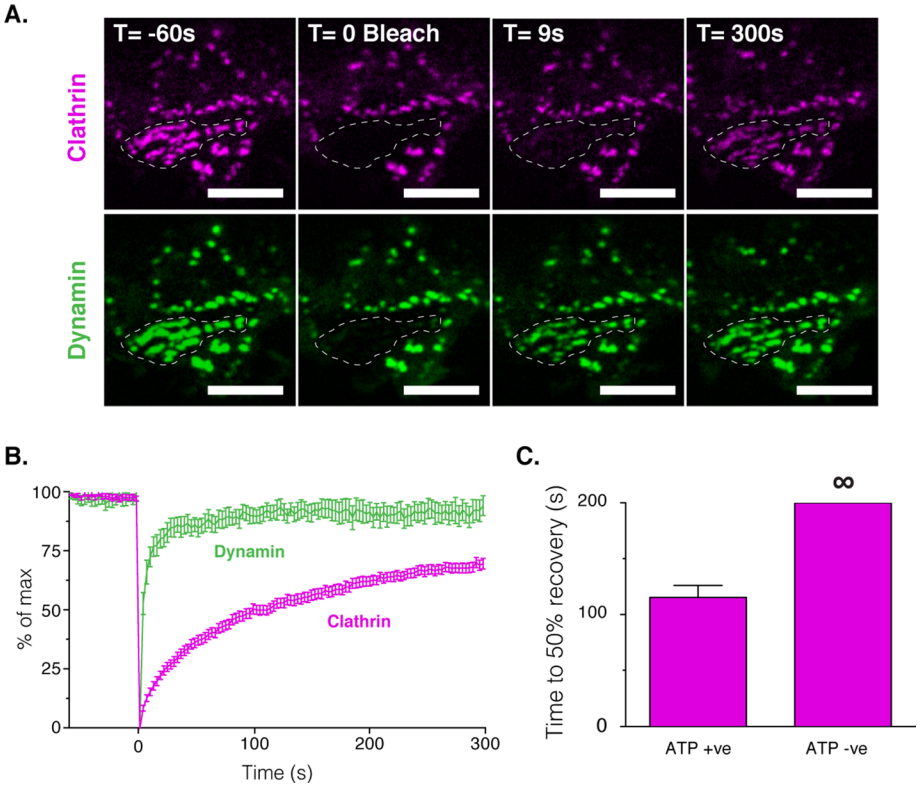

FIGURE 4: Flat clathrin lattices are dynamic molecular assemblies. HeLa cells expressing LCb-RFP and Dyn-2–EGFP were imaged by spinning disk microscopy. The fluorescence signals associated with selected groups of FCLs were photobleached, and fluorescence recovery was monitored for 10 min at 0.33 frame/s. (A) Stills from a representative experiment displaying fluorescence recovery of LCb-RFP (magenta) and Dyn-2–EGFP (green) in a selected group of FCLs (highlighted by dashed line); scale bar, 10 μm. Clathrin turnover was relatively slow, whereas dynamin exchange occurred very rapidly. (B) Mean fluorescence recovery profiles for clathrin and dynamin, $n = 32$ and 9 selected groups of FCLs, respectively; error bars indicate SEM. (C) Time to 50% recovery of clathrin fluorescence in control or ATP-depleted HeLa cells; $n = 32$ and 10 selected groups of FCLs, respectively; error bars indicate SEM.

C-terminal residues in CCR5 permits recruitment of β-arrestins, which both uncouples CCR5 from G-proteins and targets it for endocytosis via interactions with clathrin and AP-2 (Pierce and Lefkowitz, 2001; Fraile-Ramos *et al.*, 2003; Oppermann, 2004; Signoret *et al.*, 2005).

After internalization, CCR5 undergoes trafficking through the early endosome and endosomal recycling compartment to reach the *trans*-Golgi network (TGN), from where it returns to the plasma membrane in an iterative recycling loop that can persist for many hours (Signoret *et al.*, 2000, 2004; Escola *et al.*, 2010). The mechanisms regulating the plasma membrane levels of CCR5 are critical in determining cellular sensitivities to physiological ligands and coreceptor availability for HIV infection (Cocchi *et al.*, 1995; Reeves *et al.*, 2002; Oppermann, 2004). Exploiting a well-established CHO-CCR5 cell system (Mack *et al.*, 1998; Signoret *et al.*, 2000, 2004) and immunogold EM, we previously demonstrated that CCR5 associates with FCLs after stimulation with native ligand (Signoret *et al.*, 2005). Therefore we used this system to reevaluate the relationship between CCR5 and FCLs using advanced fluorescence imaging.

We first used the quantitative microscopy approaches developed in Figures 1–3 to demonstrate the existence of FCLs in CHO-CCR5 cells. As previously described (Signoret *et al.*, 2005), EM of plasma membrane sheets revealed classical CCPs as well as FCLs, often with peripheral budding structures (Supplemental Figure S4A). dSTORM recapitulated these observations (Supplemental Figure S4B), with morphometric analysis confirming two populations of CCSs—small, spherical pits and large, pleomorphic lattices (Supplemental Figure S4C) covering ~7.5% of the ventral plasma membrane (unpublished data). Live-cell TIRF microscopy of CHO-CCR5 cells expressing LCb-RFP indicated that FCLs are long-lived structures (Supplemental Figure S4D). Therefore, further to our observations in HeLa cells and in agreement with our and other reports (Miller *et al.*, 1991; Sachse *et al.*, 2001; Signoret *et al.*, 2005), large, stable FCLs are present in CHO cells.

To establish the kinetics of CCR5 internalization, we monitored receptor levels on adherent cells with a fluorescently conjugated anti-CCR5 monoclonal antibody (mAb) by live-cell microscopy (Supplemental Figure S5). Before addition of agonist, CCR5 levels remained constant; treatment with 125 nM CCL5 triggered loss of cell surface receptor, which followed an exponential decay, reaching a plateau of ~65% after 30 min. We independently verified these results by flow cytometry (Supplemental Figure S5). Of note, internalized CCR5 reaches the recycling endosome and/or TGN within 20–30 min, after which it recycles back to the plasma membrane (Signoret *et al.*, 2000; Escola *et al.*, 2010). Therefore the apparent stabilization of cell surface CCR5 by ~30 min may reflect a dynamic equilibrium in which CCR5 is simultaneously removed from and recycled back to the cell surface.

To evaluate changes in receptor distribution that accompany desensitization and internalization, we monitored the codistribution of CCR5 and clathrin by live-cell TIRF microscopy. Before treatment, antibody-labeled CCR5 was evenly distributed across the cell surface with no evidence of association with clathrin (Figure 5A, top). After stimulation with CCL5 agonist, CCR5 exhibited a gradual redistribution to CCSs, which stabilized and persisted for the duration of the study (60-min acquisition at 2 frames/min; Figure 5A and Figure 5 Video 1). We identified stable FCLs in CHO-CCR5 cells using the tracking algorithm described earlier (Figure 3B) and monitored CCR5 fluorescence associated with them over the time course. CCR5 redistribution to FCLs occurs with linear kinetics until reaching a persistent plateau at ~12 min poststimulation (Figure 5B). Preliminary FRAP analysis indicated that CCR5 association with FCLs is dynamic, with CCR5 fluorescence recovery displaying similar kinetics to clathrin turnover (unpublished data). As a further testament to the longevity of FCLs, despite subtle morphological changes, the majority of structures persevered for the entire experiment (>60 min; (Figure 5A and Figure 5 Video 1). This is also in keeping with our previous observation that agonist treatment did not affect the frequency and size of FCLs (Signoret *et al.*, 2005).

The temporal resolution used in the experiments illustrated in Figure 5, A and B, and Figure 5 Video 1 did not allow us to observe CCR5 incorporation into transient CCPs; therefore we imaged cells after 60 min of treatment using a high frame rate (10-min acquisition at 0.33 frame/s). Of importance, at 1 h posttreatment, endocytosis

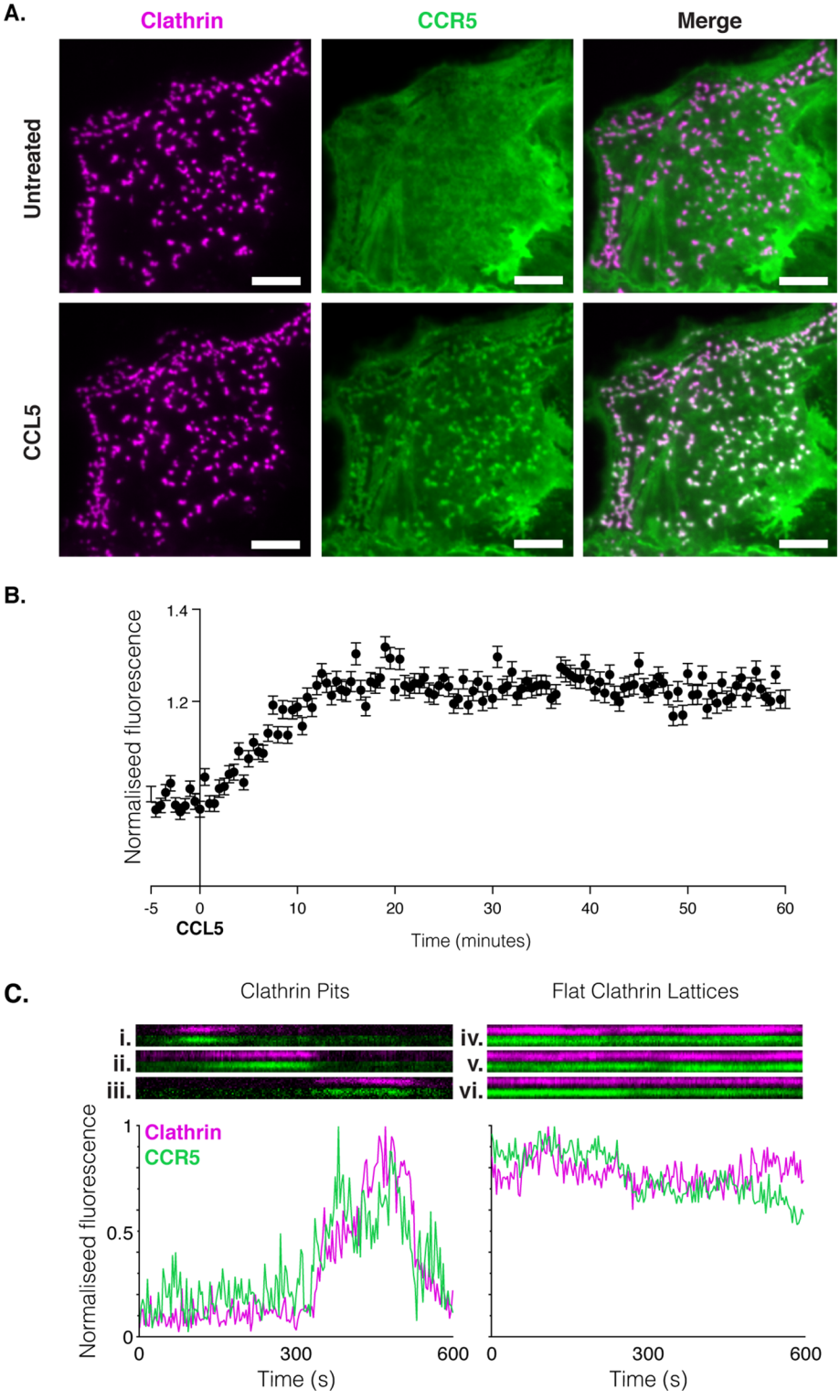

FIGURE 5: CCL5 agonist triggers persistent association of CCR5 with flat clathrin lattices. CHO-CCR5 cells expressing LCb-RFP and prelabeled with mouse anti-CCR5 mAb directly conjugated to Atto 488 were imaged by TIRF microscopy for 65 min at 2 frames/min. CCL5 was added after 5 min at a final concentration of 125 nM. (A) Images from the beginning (untreated) and end (CCL5) of a representative time course, displaying the cell surface distribution of clathrin (magenta) and CCR5 (green); scale bar, 5 μm. To better illustrate the redistribution of CCR5, the images were generated by averaging four consecutive frames from $T = 0$ and 60 min, respectively. Images without averaging can be seen in Supplemental Video 1. (B) Stable FCLs were identified using an automated tracking algorithm (see *Materials and Methods*), allowing quantification of their associated CCR5 fluorescence over the time course. The data are presented as normalized fluorescence expressed relative to the signal at $T = 0$; $n = 220$ stable FCLs from three cells, surveyed across two independent experiments; error bars indicate SEM. (C) After 60 min of treatment with CCL5 ligand, CHO-CCR5 cells were imaged for 10 min at 0.33 frame/s. Kymographs display clathrin (magenta) and CCR5 (green) signals from representative CCPs and FCLs in CHO-CCR5 cells. Line plots display normalized fluorescence intensity from the lowermost kymographs (iii, vi).

of CCR5 is ongoing due to its iterative recycling program (Signoret *et al.*, 2000; Escola *et al.*, 2010). The cell shown in Figure 5 and Figure 5 Video 2 exhibits sustained association of CCR5 with stable FCLs, alongside transient diffraction-limited CCPs that accrue receptor (boxed areas in Figure 5 Video 2). Representative kymographs (Figure 5C) display CCP- type events that simultaneously accumulate CCR5 and clathrin and stable FCLs with sustained recruitment of CCR5. This suggests that CCR5 does not discriminate between FCLs and CCPs, although, it should be noted that at any given moment, CCPs account for a minority of total plasma membrane clathrin (Figure 2 and Supplemental Figure S4).

Coupling of CCR5 to the endocytic pathway is β-arrestin dependent (Fraile-Ramos *et al.*, 2003; Truan *et al.*, 2013). However, studies of other receptor systems suggested that recruitment to CCPs and FCLs may occur via different mechanisms (Sachse *et al.*, 2001) and that GPCR may be sorted to a subset of CCSs in a β-arrestin–independent manner (Mundell *et al.*, 2006). Therefore, to evaluate the role of β-arrestin in CCR5 recruitment to FCLs, we studied GFP-tagged β-arrestin-2 in stimulated CHO-CCR5 cells by live-cell microscopy. Before treatment, β-arrestin displayed modest association with CCSs, with a large proportion appearing as a diffuse cytoplasmic signal. Stimulation with CCL5 induced a sustained association of β-arrestin-2 with CCSs (Supplemental Figure S6A and Supplemental Figure S6 Video 1). Quantification revealed that β-arrestin-2 was rapidly recruited to FCLs, reaching a plateau at ~4 min after stimulation with CCL5 (Supplemental Figure S6B).

In contrast, a β-arrestin-2 construct lacking the N-terminal domains necessary for interaction with GPCR (but possessing the requisite clathrin/AP-2–binding sites) failed to respond to CCL5 stimulation (Supplemental Figure S6B and Figure S6 Video 2). This indicates that recruitment of β-arrestin to FCLs is dependent on prior interaction with CCR5, as would be predicted by the accepted model of GPCR coupling to CME (Dewire *et al.*, 2007). Of note, this rapid CCR5-dependent sequestration of

β-arrestin-2 (Supplemental Figure S6B) may indicate the presence of CCR5 at FCLs earlier than is apparent in Figure 5. To examine this, we studied the distribution of clathrin, β-arrestin, and CCR5 on the dorsal surface of CHO cells by membrane rip-off and immunogold EM (Sanan and Anderson, 1991). In agreement with our earlier reports (Signoret *et al.*, 2005), FCLs become decorated with gold-labeled β-arrestin and CCR5 within 2 min of agonist activation (Supplemental Figure S6C), indicating that CCR5/β-arrestin complexes begin to accumulate in FCLs sooner than can be appreciated by live-cell fluorescence microscopy (Figure 5). Finally, we performed dSTORM imaging of CHO-CCR5 cells 60 min post agonist stimulation to confirm sustained recruitment of β-arrestin to the plasma membrane (Supplemental Figure S6C). In summary, after activation by agonist, CCR5 undergoes downregulation from the cell surface to ~65% of the levels in untreated cells, accompanied by rapid and sustained recruitment of CCR5/β-arrestin complexes to preexisting FCLs.

Flat clathrin lattices partition CCR5 at the plasma membrane

A number of reports suggest that FCLs may organize the cell surface distribution of both endocytic and nonendocytic receptors (Pumplin and Bloch, 1990; Miller *et al.*, 1991; Sanan and Anderson, 1991; De Deyne *et al.*, 1998; Lamaze *et al.*, 2001; Kim *et al.*, 2013). Therefore we evaluated the molecular codistribution of clathrin and CCR5 in our experimental system. To achieve this, we performed dual-color PALM/dSTORM superresolution imaging (Betzig *et al.*, 2006; Bates *et al.*, 2007; Heilemann *et al.*, 2008) of photoactivatable, GFP-tagged clathrin light chain (PAGFP-LCa) and CCR5 labeled with mAb directly conjugated to Alexa Fluor 647. In untreated cells, CCR5 was distributed throughout the plasma membrane, organized into abundant puncta that likely represent individual or small clusters of receptors (Figure 6A). Critically, there was no ostensible association with FCLs. After 60 min of treatment with CCL5, the receptors had reorganized into larger clusters often arranged in and around FCLs, leaving the remaining plasma membrane predominantly devoid of receptor (Figure 6A).

The value of localization microscopy is that it provides the positions of individual molecules as representative point coordinates that are amenable to powerful spatial statistics techniques. We evaluated the ability of FCLs to recruit endocytically active CCR5 in agonist-treated cells compared with unliganded receptor in control cells, using bivariate Hopkins analysis (Zhang *et al.*, 2006; Mattila *et al.*, 2013). A particular advantage of this method is that it generates a single value that reflects the spatial relationship between the given points; a Hopkins index of 0.5 indicates a random codistribution, a value significantly <0.5 denotes segregation, and association produces a value >0.5.

We compared the molecular point pattern of CCR5 molecules relative to the centroid positions of individual FCLs (defined as structures >100,000 nm^2) within multiple objectively chosen regions of interest. As a control, we simulated a random codistribution by replacing the positions of individual FCLs with an equal number of arbitrarily chosen points. In CCL5-treated cells, a bivariate Hopkins index of ~0.7 indicated significant association of CCR5 with FCLs (Figure 6B), consistent with the rapid and sustained recruitment observed in Figures 5 and Supplemental Figure S6 and previously reported (Signoret *et al.*, 2005). Critically, a Hopkins index of ~0.4 in untreated cells (Figure 6B) demonstrates significant segregation of CCR5 and FCLs, indicating that FCLs exclude nonactivated CCR5. Taken together, these data suggest that FCLs may provide stable platforms for the internalization and/or desensitization of GPCR.

DISCUSSION

The progressive nucleation, stabilization, and maturation of clathrin-coated pits to produce endocytic vesicles is an increasingly well understood process. In this study, we used multimodal quantitative microscopy to describe two populations of CCS—archetypal CCPs and FCLs that cannot be easily understood within the standard framework of classical CME.

Morphometric analysis by EM and dSTORM imaging (Figures 1 and 2 and Supplemental Figures S3 and S4) confirmed that small, homogeneous CCPs were present in each of the cell lines we evaluated. However, some cell types, for example, HeLa and CHO, exhibited an additional population of large, heterogeneous FCLs, similar to those observed by others in cultured cells (normal rat kidney, YT lymphocytes, HeLa, and CHO), and ex vivo primary cells (fibroblasts, adipocytes, myotubes, osteoclasts and macrophage; Heuser, 1980; Aggeler and Werb, 1982; Maupin and Pollard, 1983; Larkin *et al.*, 1986; Pumplin and Bloch, 1990; Miller *et al.*, 1991; Sanan and Anderson, 1991; Damke *et al.*, 1994; Lamaze *et al.*, 2001; Akisaka *et al.*, 2003; Bellve *et al.*, 2006; Edeling *et al.*, 2006; Vassilopoulos *et al.*, 2014). FCLs were planar (Figure 1Aiii and Supplemental Figure S3C); however, invaginating structures, indistinguishable from CCPs/CCVs, were frequently observed at their periphery (Figure 1Aiii and Supplemental Figures S3 and S4A). This is consistent with the notion that FCLs can contribute to endocytosis by producing uniform cargo-laden CCVs (Taylor *et al.*, 2011; Lampe *et al.*, 2014).

Unlike previous studies, we reconciled our ultrastructural analysis with live-cell microscopy to directly address the dynamics of FCLs (Figure 3). CCPs appeared as prototypical diffraction-limited spots with transient lifetimes ranging from 20 to 300 s. In contrast, FCLs were remarkably stable, displaying very little change in position or morphology over the duration of study (10 min; Figure 3C) and were capable of persisting for >1 h (Figure 5A). Despite this apparent stability, FRAP analysis demonstrated that FCLs are molecularly dynamic assemblies (Figure 4). We monitored dynamin association to better describe the lifetime of clathrin events. CCPs displayed a characteristic biphasic recruitment of dynamin, with an initial moderate signal, followed by an intense peak commensurate with vesicle scission (Figure 3C and Supplemental Video S1). On the contrary, FCLs exhibited sustained dynamin recruitment (Figure 3C and Supplemental Video S1), and we were unable to discern discrete peaks in intensity that might signify vesicle scission events.

The FCLs described here share some characteristics with the clathrin plaques described by Saffarian *et al.* (2009), such as planar topography and long lifetime. However, we believe that FCLs and plaques are discrete species of CCSs. Of note, clathrin plaques are comparatively small (only two to three times larger than a pit) and exhibit intermediate lifetimes (~300 s), with a burst in dynamin recruitment coordinate with endocytosis (Saffarian *et al.*, 2009). Furthermore, whereas clathrin plaques are dependent on HIP1R-mediated coupling to the actin cytoskeleton (Saffarian *et al.*, 2009), other studies suggest that flat lattices in HeLa cells are unaffected by HIP1R depletion (Engqvist-Goldstein *et al.*, 2004). Therefore clathrin plaques may represent a further subset of morphologically and kinetically distinct CCSs that form alongside FCLs and CCPs and may be present among the medium-sized flat CCSs revealed by EM and dSTORM (Figure 1 and 2). However, we were unable to analytically discriminate clathrin plaque–type events from CCPs in our live-imaging experiments (unpublished data).

To probe the relevance of FCLs to plasma membrane biology, we studied CCR5, a prototypical G protein–coupled chemokine receptor (Oppermann, 2004). Activation by a native agonist (CCL5) induced a rapid redistribution of CCR5 to FCLs that occurred in

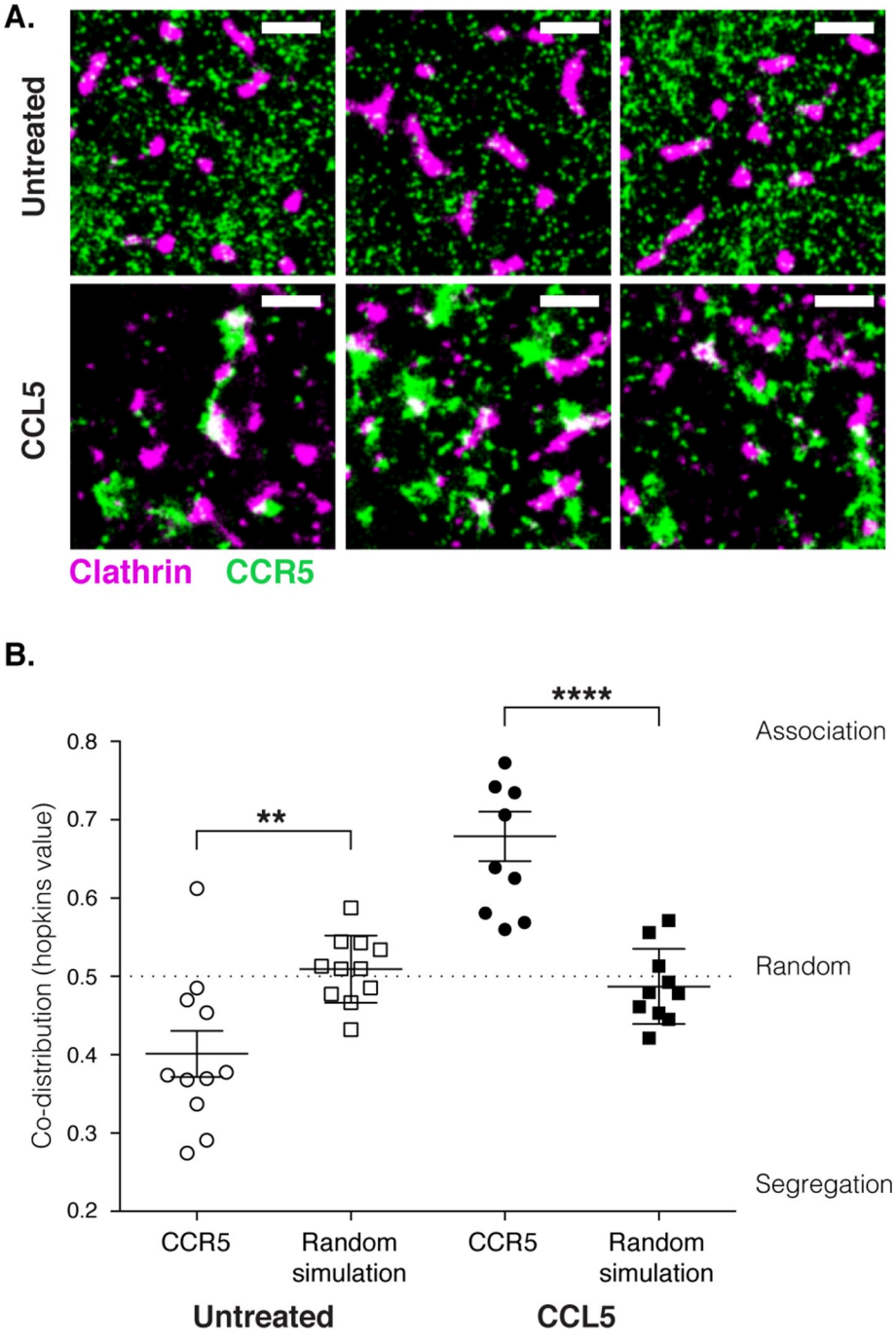

FIGURE 6: Flat clathrin lattices partition CCR5 at the plasma membrane. CHO-CCR5 cells expressing LCa-PAGFP and prelabeled with mouse anti-CCR5 mAb directly conjugated to Alexa Fluor 647 were incubated for 1 h in the presence or absence of 125 nM CCL5. Cells were fixed and imaged by two-color PALM/dSTORM. (A) Representative superresolution images of the cell surface distribution of clathrin (magenta) and CCR5 (green) in control or CCL5-treated CHO-CCR5 cells. Images were reconstructed with a 25-nm pixel size; scale bar, 1 μm. (B) The molecular codistribution of FCLs and CCR5 was quantified using Hopkins spatial statistics in multiple arbitrarily chosen regions of interest (see *Materials and Methods*). A Hopkins value of 0.5 demonstrates a random codistribution, whereas values significantly above or below 0.5 indicate association or segregation, respectively. In untreated cells, a Hopkins value of ~0.4 indicates that FCLs and CCR5 were segregated. Stimulation with CCL5 resulted in a Hopkins index of ~0.7, demonstrating association of CCR5 with FCLs. As a control, we compared the distribution of CCR5 to simulated random points, which gave a value of 0.5, indicating that the algorithm is functioning correctly. $n = 11$ (untreated) and 10 (CCL5) regions of interest, taken from three fields across two independent experiments for each condition; error bars indicate SEM; $^{**}p = 0.003$, $^{****}p \geq 0.0001$, unpaired *t* test (Prism; GraphPad, La Jolla, CA).

parallel to down-regulation of cell surface receptor (Figure 5 and Supplemental Figure S5). Liganded CCR5 remained associated with FCLs for the duration of the study (>1 h), such that FCLs dictated the cell surface distribution of activated receptor. We also observed rapid recruitment of cytoplasmic β-arrestin to FCLs (Supplemental Figure S6). Molecular codistribution analysis by localization microscopy confirmed clustering of CCR5 in and around FCLs (Figure 6). This suggests that FCLs may provide stable platforms for the recruitment of endocytic cargo, including GPCRs; this notion is supported by the recent work of Lampe *et al.* (2014) demonstrating both constitutive endocytosis of transferrin receptor and agonist-induced internalization of GPCR (β2-adrenergic receptor and Mu-opioid receptor) occurring from the same large, stable CCSs.

Clathrin sculpture

Our combined ultrastructural and live microscopy approaches demonstrate that FCLs are morphologically and kinetically distinct from standard CCP-type structures, but it remains unclear how clathrin may be fashioned into these disparate forms (Traub, 2009).

The dichotomy in clathrin phenotypes observed between HEK-293T and HeLa cells (Figures 1 and 2) suggests differentially expressed molecular determinant(s) of clathrin structure morphology. Of note, the cargo-specific adaptor Dab2 is capable of inducing very large, flat clathrin coats when overexpressed in BSC-1 cells (Mettlen *et al.*, 2010). We observed high levels of Dab2 in HeLa cells (when compared with HEK 293T) and enrichment of Dab2 within FCLs; however, small interfering RNA knockdown of Dab2 did not affect the size or frequency of FCLs (unpublished data). Identification of the factor(s) that positively or negatively regulate the formation of FCLs will likely require a comprehensive and comparative survey of FCL constituents. However, our preliminary data and observations by others suggest that FCLs contain various typical endocytic components, including some that are capable of inducing curvature to model membranes in vitro (FCHo, AP-2, epsin, Eps15; Edeling *et al.*, 2006; Hawryluk *et al.*, 2006; Hinrichsen *et al.*, 2006; unpublished data). Alternatively, adjustments to CCS topography may be regulated by a biochemical switch; for example, phosphorylation of clathrin light chain regulates the conformation of clathrin triskelia (Wilbur *et al.*, 2010; Brodsky, 2012).

Critically, FCLs were capable of producing peripheral budding structures that are morphologically indistinguishable from

CCPs/CCVs (Supplemental Figure S3). Therefore the molecular processes that dictate the geometry of classical CME must also be bought to bear on endocytic events originating from FCLs. The determinants of the uniform shape of CCVs are not fully understood but are likely to involve AP-2–dependent recruitment of AP180/CALM via NECAP (Zhang *et al.*, 1998; Meyerholz *et al.*, 2005; Aguet *et al.*, 2013; Ritter *et al.*, 2013).

Flat clathrin lattices as membrane scaffolds

Despite being first observed >30 yr ago (Heuser, 1980), the function and physiological relevance of FCLs remain unclear. This poor understanding is largely attributable to the lack of detailed characterization of FCLs; as a point of comparison, "clathrin-coated vesicle" yields >2000 PubMed results, whereas <50 articles contain information on flat clathrin structures. However, this and other studies suggest that FCLs act as stable membrane scaffolds for a variety of processes occurring at the cell surface.

FCLs likely contribute to CME by acting as endocytic platforms for various cargoes, such as GPCR, transferrin receptor, and low-density-lipoprotein receptor (Miller *et al.*, 1991; Sanan and Anderson, 1991; Lamaze *et al.*, 2001; Scott *et al.*, 2002; Signoret *et al.*, 2005; Bellve *et al.*, 2006; Lampe *et al.*, 2014). As another example, neuroendocrine cells possess extensive arrays of preformed CCSs that act as a diffusion trap to capture and internalize acetylcholine transporters after synaptic exocytosis (Sochacki *et al.*, 2012).

Beyond this conventional role in CME, we demonstrated that FCLs are able to exclude or recruit CCR5, depending on its activation status (Figure 6). This suggests that FCLs may offer a mechanism to functionally compartmentalize the plasma membrane, for example, by acting as platforms for receptor signaling and/or desensitization. In support of this concept, a recent study used dual-color superresolution imaging to show that Wnt3A stimulation induces large clathrin structures that scaffold LRP6 signaling from the cell surface (Kim *et al.*, 2013).

There are also numerous reports of a role for FCLs in cellular adhesion (Maupin and Pollard, 1983; Akisaka *et al.*, 2003; Bonazzi *et al.*, 2012), possibly via recruitment of receptors such as β1/3/5 integrins (De Deyne *et al.*, 1998; Vassilopoulos *et al.*, 2014) and nucleation of actin assembly (Akisaka *et al.*, 2008). More specifically, large, flat clathrin structures (and their associated dynamin) support actin assembly to form and maintain costameres—complexes that tether sarcomeres to the plasma membrane in skeletal muscle tissue. Knockdown of clathrin in mouse muscle leads to degeneration of myotubes, disorganized sarcomeres, and concomitant loss of muscle strength (Vassilopoulos *et al.*, 2014). These observations suggest that FCLs also act as molecular scaffolds for the transmission of mechanical force.

Many questions remain regarding the determinants and significance of clathrin heterogeneity. However, we suggest that FCLs are an underappreciated facet of plasma membrane biology. Quantitative imaging tools are likely to reveal more about nonclassical clathrin structures and the unconventional roles they play in cell biology.

MATERIALS AND METHODS

Cell culture, plasmids, and transfection

Tissue culture media and supplements were obtained from Life Technologies (Carlsbad, CA). HeLa (HEp2 strain) and HEK-293T cells were maintained in DMEM supplemented with 10% fetal calf serum, penicillin, and streptomycin; CHO-CCR5 cells (Mathias Mack, University of Regensburg, Regensburg, Germany) were maintained in α-MEM supplemented as described. Plasmids encoding LCb-RFP (Christian Merrifield, Laboratoire d'Enzymologie et Biochimie Structurales, Gif-sur-Yvette, France), Dyn-2-EGFP (Sandra Schmid, UT Southwestern Medical Center, Dallas, TX), PAGFP-LCa (Subach *et al.*, 2009), and β-arrestin-2–GFP constructs (Mark Scott, Institut Cochin, Paris, France), were introduced by transient transfection using Lipofectamine 2000 (Life Technologies).

Antibodies and reagents

The following primary antibodies were used for immunostaining: mouse anti–clathrin heavy chain X22 (Abcam, Cambridge, UK); rabbit anti–clathrin light chain immunoglobulin G (IgG; Frances Brodsky, University College London, London, United Kingdom); goat anti–dynamin-2 IgG C18 (Santa Cruz Biotechnology, Dallas, TX); mouse anti-CCR5 MC5 (Mathias Mack); rabbit anti-GFP polyclonal sera (David Shima, University College London). For live-cell labeling, anti-CCR5 MC5 was directly conjugated to either Alexa Fluor 647 (Life Technologies) or Atto 488 (Sigma-Aldrich, St. Louis, MO). All secondary antibodies were obtained from Life Technologies. Recombinant CCL5 was provided by Amanda E. I. Proudfoot (Merck Serono, Geneva, Switzerland).

Electron microscopy

Plasma membrane sheets were prepared on ice by fluid shearing (Bloch and Morrow, 1989) and rip-off methods (Sanan and Anderson, 1991; Signoret *et al.*, 2005). To prepare ventral sheets by fluid shearing, cells were grown to subconfluency on carbon-coated formvar EM grids that had been pretreated with poly-L-lysine. Samples were rinsed in HEPES buffer (25 mM 4-(2-hydroxyethyl)-1-piperazineethanesulfonic acid [HEPES], 25 mM KCl, and 2.5 mM Mg acetate, pH 7.0), and then a jet of buffer was applied across the grids from a syringe through a 25-gauge needle. This sheared the cell bodies, leaving sheets of adhered ventral membrane on the grids. To prepare dorsal sheets, we rinsed subconfluent cell monolayers grown on glass coverslips in HEPES buffer and inverted them onto EM grids, prepared as described. A rubber bung was applied to the top of the coverslips with light finger pressure for 10 s before the coverslips were lifted away, leaving portions of dorsal membrane on the EM grids. After shearing or rip-off, samples were immediately rinsed twice in HEPES buffer and fixed in 4% glutaraldehyde (or 2% formaldehyde plus 1% glutaraldehyde for immunogold labeling) and sequentially postfixed with 1% osmium tetraoxide, 10 mg/ml tannic acid, and 1.5% uranyl acetate. Membrane sheets were imaged using a Tecnai G2 Spirit transmission electron microscope (Field Emission, Hillsboro, OR) fitted with a SIS Morada charge-coupled device (CCD) camera (Olympus, Tokyo, Japan).

Superresolution imaging

For single-channel dSTORM imaging, cells were grown in four-well-chambered coverglass slides (Thermo Fisher Scientific, Waltham, MA) to low confluency. Samples were rinsed in ice-cold phosphate-buffered saline (PBS) and fixed in 4% formaldehyde plus 0.02% glutaraldehyde on ice for 10 min, followed by a further 20-min incubation at room temperature. Autofluorescence was quenched with three 5-min incubations in PBS plus 50 mM glycine. Cells were blocked/permeabilized in 0.5% bovine serum albumin (BSA) plus 0.1% Triton X-100 for 30 min and then stained sequentially with primary and secondary antibodies for 1 h with gentle rocking, interspersed by three 5-min washes in blocking buffer. dSTORM imaging was performed on an IX71 inverted microscope (Olympus), fitted with a 100×/1.49 numerical aperture (NA) TIRF objective lens (Olympus), a 150-mW, 642-nm laser (TOPTICA Photonics, Victor, NY), and an iXon 897 electron-multiplying CCD (EMCCD) camera (Andor Technology, Belfast, UK). All components were controlled with

custom software packages written in LabVIEW (National Instruments Corporation, Newbury, UK). Photoswitching buffer consisted of 1 µg/ml catalase, 50 µg/ml glucose oxidase, 40 mg/ml glucose, 12.5% glycerin, 1.25 mM KCl, 100 mM β-mercaptoethanol, and 1 mM TRIS-HCl (Metcalf *et al.*, 2013). Of importance, the imaging conditions were optimized to achieve the Nyquist sampling limit and ensure that continuous clathrin structures could be resolved.

For dual-color PALM/dSTORM imaging, CHO-CCR5 cells were grown on 25-mm coverslips and transiently transfected with PAGFP-LCa 24 h before experiments. Cell surface CCR5 was prelabeled with MC5 conjugated to Alexa Fluor 647 for 1 h on ice in binding medium (RPMI 1640 without bicarbonate containing 0.2% BSA and 10 mM HEPES, pH 7.0), after which the samples were rinsed and allowed to equilibrate to 37°C for 20 min before treatment. After stimulation with 125 nM CCL5, samples were fixed and quenched as described before mounting in an Attofluor chamber (Life Technologies) for imaging on an ELYRA PS1 (Carl Zeiss AG, Oberkochen, Germany) fitted with a 100×/1.46 NA TIRF objective; 50-mW, 405-nm, 200-mW, 488-nm, and 150-mW 642-nm lasers; and an iXon 897 EMCCD camera.

Single-channel dSTORM data were analyzed in rainSTORM (Rees *et al.*, 2013), and dual-color PALM/STORM acquisitions were analyzed in Zen 2011 (Carl Zeiss). Mean localization precision was 27.8 nm (±2.9) for dSTORM and 38.7 nm (±18.9) for PALM. Tetraspec beads (Life Technologies) were used as fiducial markers to monitor sample drift, correct chromatic offset (Erdelyi *et al.*, 2013), and perform image registration.

Live-cell imaging

For live imaging, cells were grown in four-well-chambered coverglass slides (Thermo Fisher Scientific) to low confluency and transfected with the stated fluorescent protein constructs 24 h before study. HeLa cells were imaged in standard complete medium, and CHO-CCR5 cells were imaged in binding medium (defined earlier). Studies were performed at 37°C, with and without 5% CO_2 for HeLa and CHO-CCR5 cell, respectively. TIRF microscopy was performed in a stage-mounted environmental control chamber on an N-STORM (Nikon, Tokyo, Japan) fitted with a 100×/1.49 NA TIRF objective; 220-mW, 488-nm, 110-mW, 561-nm, and 220-mW, 640-nm lasers; and an iXon 897 EMCCD camera. FRAP and spinning disk microscopy were performed in a whole-instrument environmental control chamber with an UltraVIEW VoX Yokowaga spinning disk scanner (PerkinElmer, Waltham, MA) on a TiE microscope (Nikon) fitted with a 100×/1.4 NA oil objective; 220-mW, 488-nm and 110-mW, 561-nm lasers; and a C9100-13 EMCCD camera (Hamamatsu Photonics, Hamamatsu, Japan). For live labeling, CHO-CCR5 cells were incubated with MC5-Atto 488 for 1 h on ice in binding medium, after which the cells were rinsed and allowed to equilibrate to 37°C for 20 min before study.

Morphometric analysis

We performed morphometric analysis of CCSs imaged by EM and superresolution microscopy. For EM analysis, large areas of membrane sheets were acquired by image tiling and stitching, individual clathrin structures were then identified visually and manually segmented by tracing their outlines in ImageJ (Research Services Branch, National Institutes of Health, Bethesda, MD) using a stylus and pad (Wacom Co., Kazo, Japan). Segmented structures were then used to generate binary images representing the distribution of clathrin across each membrane. For analysis by superresolution microscopy, dSTORM data were processed in rainSTORM and reconstructed as an image with a 25-nm pixel size. The CCSs in each acquisition were automatically segmented by applying a median filter with 3 × 3 pixel support and converting to a binary image. The binary data generated from EM or dSTORM images were then analyzed using the MATLAB Image Processing Toolbox (MathWorks, Natick, MA) to extract the size and shape characteristics of individual CCSs. Circularity was calculated from area and perimeter measurements using the standard circularity/roundness formula (4π area/perimeter^2).

Automated tracking

Analysis of live-cell imaging of clathrin in HeLa and CHO cells was performed in MATLAB using the u-track method (Jaqaman *et al.*, 2008; Loerke *et al.*, 2009). Briefly, CCSs were segmented using an *à trous* wavelet decomposition (Jaqaman *et al.*, 2008); the u-track software was then used to identify individual clathrin maxima within each frame and track the lifetime of individual events by linking maxima across frames. A gap-closing step ensured that tracks were not prematurely terminated by a failure in CCS detection; our analysis was performed using a maximum gap closing window of eight frames and a maximum search radius of 3 pixels, as previously validated by Jaqaman *et al.* (2008). Events that appeared for only one frame are likely to be a result of misdetection or originate from highly motile endosomal clathrin and were discarded. Events that merged or split were also rejected to avoid ambiguity in tracking and quantification. Lifetime quantification was performed on the remaining events. Representative kymographs were selected from long-lived FCLs and short-lived CCP-type events. To quantify CCR5 redistribution to FCLs, long-lived events were identified using the foregoing method, allowing their associated CCR5 signal to be monitored throughout the time course.

FRAP analysis

FRAP studies were performed on the spinning disk microscope described earlier. Photobleaching was performed using an UltraVIEW VoX PhotoKinesis device (PerkinElmer), fluorescence recovery was monitored for 5 min at 0.33 frame/s, and the data were analyzed using an ImageJ FRAP plug-in (Jeff Hardin, University of Wisconsin, Madison, WI) to extract recovery curves and calculate the time to 50% recovery.

Hopkins spatial statistics

Localization microscopy provides the positions of individual molecules in a point set data format that can be exploited to perform spatial statistics analysis. We extended the standard Hopkins algorithm (Hopkins and Skellam, 1954; Zhang *et al.*, 2006; Mattila *et al.*, 2013) to bivariate analysis of the codistribution of CCR5 and FCLs. We used a custom MATLAB routine to compare the molecular point distribution of CCR5 to the centroid positions of FCLs (identified using the morphometric analysis method outlined earlier and defined as structures of >100,000 nm^2). Multiple nonoverlapping rectangular regions of interest were chosen semiarbitrarily to include continuous areas of plasma membrane and exclude cell edges or cell–cell junctions; the mean size of the regions was 150 µm^2. Two control situations were used: the analysis was repeated, but the centroid positions of FCLs were replaced by an equal number of randomly chosen points (Figure 6), or CCR5 localization data were compared with the positions of FCLs that had been rotated 90° around a central point to disrupt any spatial relationship. In both cases the Hopkins analysis indicated a random distribution (Figure 6; unpublished data), indicating that the algorithm was functioning correctly.

Topographic analysis of CCSs

We inferred topographical information from CCSs imaged by electron microscopy by systematically measuring the electron intensity profile across individual structures. The mean electron intensity signal across CCPs (defined as structures with area <30,000 nm^2 and circularity >0.7) and FCLs (area >100,000 nm^2) was measured using the ImageJ radial profile plot plug-in (Pål Baggethun, Elkem Technology, Kristiansand, Norway). The profile was measured across a 100-nm radius from the centroid positions of CCPs and a 500-nm radius from that of FCLs. Budding structures at the periphery of FCLs were defined as invaginations occurring ≤50 nm from the edge of a lattice and were then analyzed using a 100-nm profile radius.

ACKNOWLEDGMENTS

We thank colleagues in the MRC, Laboratory for Molecular Cell Biology and National Physical Laboratory for ongoing discussions during the development of this work and Frances Brodsky, Annegret Pelchen-Matthews, Ricardo Henriques, and Chris Stefan for critically reading the manuscript. We also acknowledge Janos Kriston-Vizi and Schuyler Van Engelenburg for technical assistance. This work was funded by UK Medical Research Council core funding to the MRC-University College London Laboratory for Molecular Cell Biology University Unit (Grant MC_U122665002), a short-term fellowship to J.G. from the European Molecular Biology Organization, and the Royal Free Charity.

REFERENCES

Aggeler J, Werb Z (1982). Initial events during phagocytosis by macrophages viewed from outside and inside the cell: membrane-particle interactions and clathrin. J Cell Biol 94, 613–623.

Aguet F, Antonescu CN, Mettlen M, Schmid SL, Danuser G (2013). Advances in analysis of low signal-to-noise images link dynamin and AP2 to the functions of an endocytic checkpoint. Dev Cell 26, 279–291.

Akisaka T, Yoshida H, Suzuki R, Shimizu K, Takama K (2003). Clathrin sheets on the protoplasmic surface of ventral membranes of osteoclasts in culture. J Electron Microsc (Tokyo) 52, 535–543.

Akisaka T, Yoshida H, Suzuki R, Takama K (2008). Adhesion structures and their cytoskeleton-membrane interactions at podosomes of osteoclasts in culture. Cell Tissue Res 331, 625–641.

Bates M, Huang B, Dempsey GT, Zhuang X (2007). Multicolor super-resolution imaging with photo-switchable fluorescent probes. Science 317, 1749–1753.

Bellve KD, Leonard D, Standley C, Lifshitz LM, Tuft RA, Hayakawa A, Corvera S, Fogarty KE (2006). Plasma membrane domains specialized for clathrin-mediated endocytosis in primary cells. J Biol Chem 281, 16139–16146.

Betzig E, Patterson GH, Sougrat R, Lindwasser OW, Olenych S, Bonifacino JS, Davidson MW, Lippincott-Schwartz J, Hess HF (2006). Imaging intracellular fluorescent proteins at nanometer resolution. Science 313, 1642–1645.

Bloch RJ, Morrow JS (1989). An unusual beta-spectrin associated with clustered acetylcholine receptors. J Cell Biol 108, 481–493.

Böcking T, Aguet F, Harrison SC, Kirchhausen T (2011). Single-molecule analysis of a molecular disassemblase reveals the mechanism of Hsc70-driven clathrin uncoating. Nat Struct Mol Biol 18, 295–301.

Bonazzi M, Kühbacher A, Toledo-Arana A, Mallet A, Vasudevan L, Pizarro-Cerdá J, Brodsky FM, Cossart P (2012). A common clathrin-mediated machinery co-ordinates cell-cell adhesion and bacterial internalization. Traffic 13, 1653–1666.

Brodsky FM (2012). Diversity of clathrin function: new tricks for an old protein. Annu Rev Cell Dev Biol 28, 309–336.

Cocchi F, DeVico AL, Garzino-Demo A, Arya SK, Gallo RC, Lusso P (1995). Identification of RANTES, MIP-1 alpha, and MIP-1 beta as the major HIV-suppressive factors produced by CD8+ T cells. Science 270, 1811–1815.

Cocucci E, Aguet F, Boulant S, Kirchhausen T (2012). The first five seconds in the life of a clathrin-coated pit. Cell 150, 495–507.

Damke H, Baba T, Warnock DE, Schmid SL (1994). Induction of mutant dynamin specifically blocks endocytic coated vesicle formation. J Cell Biol 127, 915–934.

De Deyne PG, O'Neill A, Resneck WG, Dmytrenko GM, Pumplin DW, Bloch RJ (1998). The vitronectin receptor associates with clathrin-coated membrane domains via the cytoplasmic domain of its beta5 subunit. J Cell Sci 111, 2729–2740.

Dewire SM, Ahn S, Lefkowitz RJ, Shenoy SK (2007). Beta-arrestins and cell signaling. Annu Rev Physiol 69, 483–510.

Dragic T, Litwin V, Allaway GP, Martin SR, Huang Y, Nagashima KA, Cayanan C, Maddon PJ, Koup RA, Moore JP, *et al*. (1996). HIV-1 entry into CD4+ cells is mediated by the chemokine receptor CC-CKR-5. Nature 381, 667–673.

Edeling MA, Mishra SK, Keyel PA, Steinhauser AL, Collins BM, Roth R, Heuser JE, Owen DJ, Traub LM (2006). Molecular switches involving the AP-2 beta2 appendage regulate endocytic cargo selection and clathrin coat assembly. Dev Cell 10, 329–342.

Ehrlich M, Boll W, Van Oijen A, Hariharan R, Chandran K, Nibert ML, Kirchhausen T (2004). Endocytosis by random initiation and stabilization of clathrin-coated pits. Cell 118, 591–605.

Engqvist-Goldstein AEY, Zhang CX, Carreno S, Barroso C, Heuser JE, Drubin DG (2004). RNAi-mediated Hip1R silencing results in stable association between the endocytic machinery and the actin assembly machinery. Mol Biol Cell 15, 1666–1679.

Erdelyi M, Rees E, Metcalf D, Schierle GSK, Dudas L, Sinko J, Knight AE, Kaminski CF (2013). Correcting chromatic offset in multicolor super-resolution localization microscopy. Opt Express 21, 10978–10988.

Escola JM, Kuenzi G, Gaertner H, Foti M, Hartley O (2010). CC chemokine receptor 5 (CCR5) Desensitization: cycling receptors accumulate in the trans-golgi network. J Biol Chem 285, 41772–41780.

Fraile-Ramos A, Kohout TA, Waldhoer M, Marsh M (2003). Endocytosis of the viral chemokine receptor US28 does not require beta-arrestins but is dependent on the clathrin-mediated pathway. Traffic 4, 243–253.

Gaidarov I, Santini F, Warren RA, Keen JH (1999). Spatial control of coated-pit dynamics in living cells. Nat Cell Biol 1, 1–7.

Grassart A, Cheng AT, Hong SH, Zhang F, Zenzer N, Feng Y, Briner DM, Davis GD, Malkov D, Drubin DG (2014). Actin and dynamin2 dynamics and interplay during clathrin-mediated endocytosis. J Cell Biol 205, 721–735.

Greene LE, Eisenberg E (1990). Dissociation of clathrin from coated vesicles by the uncoating Atpase. J Biol Chem 265, 6682–6687.

Hawryluk MJ, Keyel PA, Mishra SK, Watkins SC, Heuser JE, Traub LM (2006). Epsin 1 is a polyubiquitin-selective clathrin-associated sorting protein. Traffic 7, 262–281.

Heilemann M, van de Linde S, Schüttpelz M, Kasper R, Seefeldt B, Mukherjee A, Tinnefeld P, Sauer M (2008). Subdiffraction-resolution fluorescence imaging with conventional fluorescent probes. Angew Chem Int Ed Engl 47, 6172–6176.

Henne WM, Boucrot E, Meinecke M, Evergren E, Vallis Y, Mittal R, McMahon HT (2010). FCHo proteins are nucleators of clathrin-mediated endocytosis. Science 328, 1281–1284.

Heuser J (1980). Three-dimensional visualization of coated vesicle formation in fibroblasts. J Cell Biol 84, 560–583.

Heuser J (1989). Effects of cytoplasmic acidification on clathrin lattice morphology. J Cell Biol 108, 401–411.

Heuser J (2000). The production of "cell cortices" for light and electron microscopy. Traffic 1, 545–552.

Hinrichsen L, Meyerholz A, Groos S, Ungewickell EJ (2006). Bending a membrane: how clathrin affects budding. Proc Natl Acad Sci USA 103, 8715–8720.

Hoffmann A, Dannhauser PN, Groos S, Hinrichsen L, Curth U, Ungewickell EJ (2010). A comparison of GFP-tagged clathrin light chains with fluorochromated light chains in vivo and in vitro. Traffic 11, 1129–1140.

Hopkins B, Skellam JG (1954). A new method for determining the type of distribution of plant individuals. Ann Botany 18, 213–227.

Jaqaman K, Loerke D, Mettlen M, Kuwata H, Grinstein S, Schmid SL, Danuser G (2008). Robust single-particle tracking in live-cell time-lapse sequences. Nat Methods 5, 695–702.

Kanaseki T, Kadota K (1969). The "vesicle in a basket." A morphological study of the coated vesicle isolated from the nerve endings of the guinea pig brain, with special reference to the mechanism of membrane movements. J Cell Biol 42, 202–220.

Kim I, Pan W, Jones SA, Zhang Y, Zhuang X, Wu D (2013). Clathrin and AP2 are required for PtdIns(4,5)P2-mediated formation of LRP6 signalosomes. J Cell Biol 200, 419–428.

Kleist von L, Stahlschmidt W, Bulut H, Gromova K, Puchkov D, Robertson MJ, Macgregor KA, Tomlin N, Pechstein A, Chau N, *et al*. (2011). Role of the clathrin terminal domain in regulating coated pit dynamics revealed by small molecule inhibition. Cell 146, 471–484.

Lamaze C, Dujeancourt A, Baba T, Lo CG, Benmerah A, Dautry-Varsat A (2001). Interleukin 2 receptors and detergent-resistant membrane domains define a clathrin-independent endocytic pathway. Mol Cell 7, 661–671.
Lampe M, Pierre F, Al-Sabah S, Krasel C, Merrifield CJ (2014). Dual single scission event analysis of constitutive transferrin receptor (TfR) endocytosis and ligand-triggered β2-adrenergic receptor (β2AR) or Mu-opioid receptor (MOR) endocytosis. Mol Biol Cell 25, 3070–3080.
Larkin JM, Donzell WC, Anderson RG (1986). Potassium-dependent assembly of coated pits: new coated pits form as planar clathrin lattices. J Cell Biol 103, 2619–2627.
Loerke D, Mettlen M, Yarar D, Jaqaman K, Jaqaman H, Danuser G, Schmid SL (2009). Cargo and dynamin regulate clathrin-coated pit maturation. PLoS Biol 7, e57.
Macia E, Ehrlich M, Massol R, Boucrot E, Brunner C, Kirchhausen T (2006). Dynasore, a cell-permeable inhibitor of dynamin. Dev Cell 10, 839–850.
Mack M, Luckow B, Nelson PJ, Cihak J, Simmons G, Clapham PR, Signoret N, Marsh M, Stangassinger M, Borlat F, *et al*. (1998). Aminooxypentane-RANTES induces CCR5 internalization but inhibits recycling: a novel inhibitory mechanism of HIV infectivity. J Exp Med 187, 1215–1224.
Marsh M, McMahon HT (1999). The structural era of endocytosis. Science 285, 215–220.
Mattila PK, Feest C, Depoil D, Treanor B, Montaner B, Otipoby KL, Carter R, Justement LB, Bruckbauer A, Batista FD (2013). The actin and tetraspanin networks organize receptor nanoclusters to regulate B cell receptor-mediated signaling. Immunity 38, 461–474.
Maupin P, Pollard TD (1983). Improved preservation and staining of HeLa cell actin filaments, clathrin-coated membranes, and other cytoplasmic structures by tannic acid-glutaraldehyde-saponin fixation. J Cell Biol 96, 51–62.
McMahon HT, Boucrot E (2011). Molecular mechanism and physiological functions of clathrin-mediated endocytosis. Nat Rev Mol Cell Biol 12, 517–533.
Merrifield CJ, Feldman ME, Wan L, Almers W (2002). Imaging actin and dynamin recruitment during invagination of single clathrin-coated pits. Nat Cell Biol 4, 691–698.
Merrifield CJ, Perrais D, Zenisek D (2005). Coupling between clathrin-coated-pit invagination, cortactin recruitment, and membrane scission observed in live cells. Cell 121, 593–606.
Metcalf DJ, Edwards R, Kumarswami N, Knight AE (2013). Test samples for optimizing STORM super-resolution microscopy. J Vis Exp 79, e50579.
Mettlen M, Loerke D, Yarar D, Danuser G, Schmid SL (2010). Cargo- and adaptor-specific mechanisms regulate clathrin-mediated endocytosis. J Cell Biol 188, 919–933.
Meyerholz A, Hinrichsen L, Groos S, Esk P-C, Brandes G, Ungewickell EJ (2005). Effect of clathrin assembly lymphoid myeloid leukemia protein depletion on clathrin coat formation. Traffic 6, 1225–1234.
Miller K, Shipman M, Trowbridge IS, Hopkins CR (1991). Transferrin receptors promote the formation of clathrin lattices. Cell 65, 621–632.
Mundell SJ, Luo J, Benovic JL, Conley PB, Poole AW (2006). Distinct clathrin-coated pits sort different G protein-coupled receptor cargo. Traffic 7, 1420–1431.
Nicol A, Nermut MV (1987). A new type of substratum adhesion structure in NRK cells revealed by correlated interference reflection and electron microscopy. Eur J Cell Biol 43, 348–357.
Oppermann M (2004). Chemokine receptor CCR5: insights into structure, function, and regulation. Cell Signal 16, 1201–1210.
Otter, Den WK, Briels WJ (2011). The generation of curved clathrin coats from flat plaques. Traffic 12, 1407–1416.
Pierce KL, Lefkowitz RJ (2001). Classical and new roles of beta-arrestins in the regulation of G-protein-coupled receptors. Nat Rev Neurosci 2, 727–733.
Pumplin DW, Bloch RJ (1990). Clathrin-coated membrane: a distinct membrane domain in acetylcholine receptor clusters of rat myotubes. Cell Motil Cytoskeleton 15, 121–134.
Rappoport JZ, Simon SM (2003). Real-time analysis of clathrin-mediated endocytosis during cell migration. J Cell Sci 116, 847–855.
Rappoport JZ, Simon SM, Benmerah A, (2004). Understanding living clathrin-coated pits. Traffic 5, 327–337.
Rees EJ, Erdelyi M, Schierle GSK, Knight A, Kaminski CF (2013). Elements of image processing in localization microscopy. J Opt 15, 094012.
Reeves JD, Gallo SA, Ahmad N, Miamidian JL, Harvey PE, Sharron M, Pohlmann S, Sfakianos JN, Derdeyn CA, Blumenthal R, *et al*. (2002). Sensitivity of HIV-1 to entry inhibitors correlates with envelope/coreceptor affinity, receptor density, and fusion kinetics. Proc Natl Acad Sci USA 99, 16249–16254.
Ritter B, Murphy S, Dokainish H, Girard M, Gudheti MV, Kozlov G, Halin M, Philie J, Jorgensen EM, Gehring K, *et al*. (2013). NECAP 1 regulates AP-2 Interactions to control vesicle size, number, and cargo during clathrin-mediated endocytosis. PLoS Biol 11, e1001670.
Sachse M, van Kerkhof P, Strous GJ, Klumperman J (2001). The ubiquitin-dependent endocytosis motif is required for efficient incorporation of growth hormone receptor in clathrin-coated pits, but not clathrin-coated lattices. J Cell Sci 114, 3943–3952.
Saffarian S, Cocucci E, Kirchhausen T (2009). Distinct dynamics of endocytic clathrin-coated pits and coated plaques. PLoS Biol 7, e1000191.
Sanan DA, Anderson RG (1991). Simultaneous visualization of LDL receptor distribution and clathrin lattices on membranes torn from the upper surface of cultured cells. J Histochem Cytochem 39, 1017–1024.
Schlossman DM, Schmid SL, Braell WA, Rothman JE (1984). An enzyme that removes clathrin coats—purification of an uncoating Atpase. J Cell Biol 99, 723–733.
Scott MGH, Benmerah A, Muntaner O, Marullo S (2002). Recruitment of activated G protein-coupled receptors to pre-existing clathrin-coated pits in living cells. J Biol Chem 277, 3552–3559.
Signoret N, Christophe T, Oppermann M, Marsh M (2004). pH-Independent endocytic cycling of the chemokine receptor CCR5. Traffic 5, 529–543.
Signoret N, Hewlett L, Wavre S, Pelchen-Matthews A, Oppermann M, Marsh M (2005). Agonist-induced endocytosis of CC chemokine receptor 5 is clathrin dependent. Mol Biol Cell 16, 902–917.
Signoret N, Pelchen-Matthews A, Mack M, Proudfoot AE, Marsh M (2000). Endocytosis and recycling of the HIV coreceptor CCR5. J Cell Biol 151, 1281–1294.
Smith CJ, Grigorieff N, Pearse BM (1998). Clathrin coats at 21 A resolution: a cellular assembly designed to recycle multiple membrane receptors. EMBO J 17, 4943–4953.
Sochacki KA, Larson BT, Sengupta DC, Daniels MP, Shtengel G, Hess HF, Taraska JW (2012). Imaging the post-fusion release and capture of a vesicle membrane protein. Nat Commun 3, 1154.
Subach FV, Patterson GH, Manley S, Gillette JM, Lippincott-Schwartz J, Verkhusha VV (2009). Photoactivatable mCherry for high-resolution two-color fluorescence microscopy. Nat Methods 6, 153–159.
Taylor MJ, Lampe M, Merrifield CJ (2012). A feedback loop between dynamin and actin recruitment during clathrin-mediated endocytosis. PLoS Biol 10, e1001302.
Taylor MJ, Perrais D, Merrifield CJ (2011). A high precision survey of the molecular dynamics of Mammalian clathrin-mediated endocytosis. PLoS Biol 9, e1000604.
Traub LM (2009). Clathrin couture: fashioning distinctive membrane coats at the cell surface. PLoS Biol 7, e1000192.
Truan Z, Tarancón Díez L, Bönsch C, Malkusch S, Endesfelder U, Munteanu M, Hartley O, Heilemann M, Fürstenberg A (2013). Quantitative morphological analysis of arrestin2 clustering upon G protein-coupled receptor stimulation by super-resolution microscopy. J Struct Biol 184, 329–334.
Ungewickell E, Ungewickell H, Holstein SE, Lindner R, Prasad K, Barouch W, Martin B, Greene LE, Eisenberg E (1995). Role of auxilin in uncoating clathrin-coated vesicles. Nature 378, 632–635.
Vassilopoulos S, Gentil C, Lainé J, Buclez P-O, Franck A, Ferry A, Précigout G, Roth R, Heuser JE, Brodsky FM, *et al*. (2014). Actin scaffolding by clathrin heavy chain is required for skeletal muscle sarcomere organization. J Cell Biol 205, 377–393.
Warnock DE, Baba T, Schmid SL (1997). Ubiquitously expressed dynamin-II has a higher intrinsic GTPase activity and a greater propensity for self-assembly than neuronal dynamin-I. Mol Biol Cell 8, 2553–2562.
Wilbur JD, Hwang PK, Ybe JA, Lane M, Sellers BD, Jacobson MP, Fletterick RJ, Brodsky FM (2010). Conformation switching of clathrin light chain regulates clathrin lattice assembly. Dev Cell 18, 841–848.
Wu X, Zhao X, Baylor L, Kaushal S, Eisenberg E, Greene LE (2001). Clathrin exchange during clathrin-mediated endocytosis. J Cell Biol 155, 291–300.
Wu X, Zhao X, Puertollano R, Bonifacino JS, Eisenberg E, Greene LE (2003). Adaptor and clathrin exchange at the plasma membrane and trans-Golgi network. Mol Biol Cell 14, 516–528.
Zhang B, Koh YH, Beckstead RB, Budnik V, Ganetzky B, Bellen HJ (1998). Synaptic vesicle size and number are regulated by a clathrin adaptor protein required for endocytosis. Neuron 21, 1465–1475.
Zhang J, Leiderman K, Pfeiffer JR, Wilson BS, Oliver JM, Steinberg SL (2006). Characterizing the topography of membrane receptors and signaling molecules from spatial patterns obtained using nanometer-scale electron-dense probes and electron microscopy. Micron 37, 14–34.